The geomagnetic dipole moment variation between 250 and 800 ka BP reconstructed from the authigenic $^{10}Be/^{9}Be$ signature in West Equatorial Pacific sediments

Lucie Ménabréaz *, Nicolas Thouveny, Didier L. Bourlès, Laurence Vidal

Aix-Marseille Université, CNRS, IRD, CEREGE UM 34, Technopôle de l'Environnement Arbois-Méditerranée, BP80, 13545 Aix-en-Provence, France

Keywords:

marine sediment geochemistr, ^{10}Be cosmogenic production, geomagnetic dipole moment , Brunhes paleomagnetic excursions Brunhes/Matuyama transition

The authigenic $^{10}Be/^{9}Be$ ratio, proxy of the cosmogenic radionuclide ^{10}Be production rate in the atmosphere, was measured in sediments deposited in the West Equatorial Pacific (Gulf of Papua; 10°25 S; 146°15 E), in order to reconstruct the geomagnetic dipole moment variations in the 250–800 ka time interval, independently from paleomagnetic methods. The pelagic clayey-carbonate muds continuously deposited between marine isotope stages 8 and 20 were subsampled every 10 cm. The ^{10}Be production rate record reconstructed for the 250–800 ka interval is described and compared over the same time interval with global paleomagnetic stacks (SINT-2000 and PISO-1500). The highlighted cosmogenic ^{10}Be overproductions appear to be triggered by the series of Geomagnetic Dipole Lows (GDL) that have occurred since the Brunhes–Matuyama reversal. Calibration using absolute values of the geomagnetic dipole moment drawn from a paleomagnetic database produces a new record of the dipole moment variations over the 250–800 ka time interval. The timing and amplitude of the GDL succession revealed by such records will contribute to improving knowledge of the geodynamo rhythms and rate of changes at millennial to million year scales.

1. Introduction

Reconstructing past intensity variations in the Earth's magnetic field over the last million years is necessary in order to better understand planetary magnetic field dynamics, and hence the processes that govern the geodynamo. Accurate records of past geodynamo rhythms are also fundamental to understand present-day geomagnetic field behaviour, and thus to better predict its future dynamics and adapt our societal responses. Current knowledge about the geomagnetic dipole moment variation at millennial or longer time scales has until now been deduced mainly from paleomagnetic investigations. Relative PaleoIntensity (RPI) variations recorded in sediment archives provide nearly continuous time series of the Virtual (Axial) Dipole Moment (V(A)DM), while paleointensity determinations performed on lava flows provide discontinuous series of absolute V(A)DM values (see Tauxe, 1993 and Valet, 2003 for comprehensive reviews).

Sedimentary paleomagnetic records can, however, be biased by magnetization acquisition processes such as delayed remanence acquisition and/or progressive magnetization lock-in after sediment deposition (e.g. Coe and Liddicoat, 1994; Roberts and Winklhofer, 2004). Normalized intensity records can also be affected by paleoclimatic and paleoenvironmental contamination. This has led to questioning of the geomagnetic significance of relative paleointensity records (e.g. Channell et al., 1998; Guyodo et al., 2000; Xuan and Channell, 2008) and to the development of strategies to reduce such influences (e.g. Tauxe et al., 2006; Hofmann and Fabian, 2009).

The most common strategy consists in compiling single RPI records obtained from several varied sediment sequences, and using statistical filtering and smoothing methods to produce mean normalized RPI records of regional or global significance. Such regional stacks (e.g. Laj et al., 2000; Stoner et al., 2002; Thouveny et al., 2004; Yamazaki and Oda, 2002) or global stacks (e.g. Guyodo and Valet, 1999; Laj et al., 2004; Valet et al., 2005; Channell et al., 2009) are generally calibrated using absolute VDM (or VADM) values obtained from absolute paleointensity data sets and are thus expressed in 10^{22} Am^2. These stacks produce consistent dipole moment variations over the last million years that satisfactorily correlate with the series of magnetic anomalies recorded from the South-East Pacific seafloor by Gee et al. (2000) (e.g. Fig. 2 of Thouveny et al., 2008). Furthermore, the chronological agreement between minimum dipole moment signals and well-known excursions and reversals (e.g. Valet, 2003; Laj and Channell, 2007; Thouveny et al., 2008) confirms their accuracy as proxies of the geomagnetic dipole lows. Spectral analyses of these stacks reveal periods in the same range as orbital parameters, reintroducing

* Corresponding author. Tel.: +33 04 42 97 15 08; fax: +33 04 42 97 15 95.
E-mail address: menabreaz@cerege.fr (L. Ménabréaz).

the hypothesis of an orbital influence on the geodynamo (e.g. Xuan and Channell, 2008; Fuller, 2006; Thouveny et al., 2008; Saracco et al., 2009). However, detailed comparison between the different dipole moment reconstructions points out noticeable amplitude discrepancies and chronological mismatches.

The current debates surrounding these results, as well as the limited understanding of the physical processes controlling magnetization acquisition in sediments and lavas, highlight the need to reconstruct dipole field intensity variations using an independent approach, integrating the global-scale magnetospheric signal.

For these purposes, studies of the variations of the cosmogenic nuclide Beryllium-10 (^{10}Be, half-life ~ 1.4 Ma) atmospheric production rate have recently been performed. At millennial or longer timescales, the geomagnetic dipole moment that modulates the galactic cosmic ray flux penetrating the Earth's environment undoubtedly constitutes the main modulation factor of the global atmospheric ^{10}Be production rate (e.g. Elsasser et al., 1956; Lal, 1988; Wagner et al., 2000; Masarik and Beer 1999, 2009). Once atmospherically produced, ^{10}Be is rapidly transferred through precipitations to the Earth's surface (Raisbeck et al., 1981; Bourlès, 1992; Baroni et al., 2011), where it accumulates in natural archives that thus record the production rate variations. Using ^{10}Be atmospheric transport modelling, Heikkilä et al. (2009, 2013) have shown that the stratospheric, well-mixed fraction of ^{10}Be is always dominant in worldwide ^{10}Be depositional fluxes. These results have been reinforced by the reproducibility and synchronicity of ^{10}Be production records in Greenland ice and in mid- to low-latitude marine sediments over the 20–50 ka time interval (Ménabréaz et al., 2012), further strengthening the earlier assumption that long-term changes in ^{10}Be fluxes recorded in ice sheets reflect a geomagnetic signal modulation (e.g. Muscheler et al. 2004, 2005; Wagner et al., 2000). Evidence of this modulation over the past million years are documented by ^{10}Be fluxes in ice cores (e.g. Raisbeck et al., 1992; Finkel and Nishiizumi, 1997; Yiou et al., 1997; Muscheler et al., 2005; Raisbeck et al., 2006) and in marine sediments, using either ^{10}Be/^{230}Th$_{xs}$ (e.g. Frank et al., 1997; Christl et al. 2003, 2007, 2010; Ménabréaz et al., 2011; Fig. 1A) or ^{10}Be/^{9}Be of the authigenic fraction – i.e. fraction due to the adsorption onto settling particles – (e.g. Raisbeck et al., 1985; Henken-Mellies et al., 1990; Robinson et al., 1995; Carcaillet et al. 2003, 2004a, 2004b; Ménabréaz et al., 2011, 2012; Fig. 1A) in order to correct for the environmental biases due to oceanic transport processes. The fundamentals of these two normalization methods, as well as their possible associated biases, have been discussed in e.g. François et al. (2004) and Ménabréaz et al. (2011, 2012), respectively. In the latter studies, it has been proven that the authigenic ^{10}Be/^{9}Be methodology, notably confirmed by a ^{10}Be/^{230}Th$_{xs}$ cross-evaluation, reliably corrects for ocean secondary contributions. Most of the available records span the last 250–300 ka, as the use of ^{230}Th$_{xs}$ as a constant flux proxy is limited to 350 ka due to the ^{230}Th half-life (75 690 yr; e.g. Henderson and Anderson, 2003). This is not the case for the authigenic ^{10}Be/^{9}Be method, which is limited, at most, to the last 14 Ma due to ^{10}Be radioactive decay. Authigenic ^{10}Be/^{9}Be studies are, however, scarce, and there are no data documenting the cosmogenic nuclide production rate variations during the 300–500 ka time period, and a few measurement data points were obtained over the 500–800 ka time period (Carcaillet et al., 2003).

Here, we present an authigenic ^{10}Be/^{9}Be record from a deep-sea sediment core which documents ^{10}Be global atmospheric production rate changes between 250 and 800 ka (and which thus includes the last geomagnetic reversal at about 780 ka) and we aim to reconstruct the associated dipole moment variations, notably those accompanying excursions and reversal. The studied core was retrieved near the equator, where the geomagnetic modulation of the galactic cosmic ray flux is the most efficient. The choice of a study area on a continental margin (Gulf of Papua; Fig. 1) is justified by a high vertical particle flux not only minimizing the Be residence time with respect to scavenging, but also reducing the effects of mixing in the water column and the influence of bioturbation processes, and hence of ^{10}Be signal attenuation and shifting (see for example Christl, 2007; Ménabréaz et al., 2012).

2. Materials and methods

2.1. Environmental setting of core MD05-2930

The Gulf of Papua (GOP) comprises an ~ 150 000 km^2 area south of Papua New Guinea, east of the Torres Strait (Fig. 1B and C). The GOP continental shelf is wide to the West and Northwest (~ 200 km) and narrows to the Northeast (~ 10–30 km). Several major rivers drain southern Papua New Guinea Island, of which the Fly, Kikori and Purari Rivers currently discharge 200 to 400 megatons per year of terrigeneous siliciclastic material, mainly deposited onto the inner shelf of the GOP (Harris et al., 1993; Milliman, 1995). To this large volume of siliciclastic sediments are added important sources of neritic carbonates (see Francis et al., 2008 and references therein) that can produce up to 10 to 20 Mt per year of carbonate detrital particles (Dickens et al., 2006). Car-bonate sedimentation in the GOP originates firstly from the north-ern extension of the Great Barrier Reef, which covers the western GOP shelf. This reef system is at present composed of a nearly continuous barrier reef along the shelf break, with patch reefs in the inner and middle shelves toward the southern Fly River delta. Secondly, isolated Miocene carbonate platforms evolved into large atolls during the Pleistocene (Ashmore, Boot, Portlock and East-ern Fields Reefs). Given the continental margin's shallow water depth (0 to 125 m), the Pleistocene sea-level fluctuations influenced the nature and rhythm of the GOP sedimentation (see Jorry et al., 2008). During sea-level lowstands (Glacials), the continental shelf was subaerially exposed, the main rivers extended to the present shelf edge and reef systems karstified. This led to an increased dilution of the carbonate fluxes by the siliciclastic fluxes.

The MD05-2930 core (10°25 S; 146°15 E; Fig. 1C) was collected at 1490 m water depth on an intra-slope bathymetric plateau (Eastern Plateau, ~ 25 000 km^2; see Francis et al., 2008), dominated by a siliciclastic sedimentation, with less than 40% carbonates during the last glacial–interglacial cycles (e.g. McFadden et al., 2006). This 36.88 m long core was retrieved using a giant CALYPSO piston corer on board of the R/V *Marion Dufresne* (MD-148 PECTEN Cruise, 2005). The sediment sequence is mainly composed of homogeneous grey–green clayey and silty clayey muds, rich in foraminifera (Beaufort et al., 2005).

2.2. Chronostratigraphic framework

Benthic foraminifera, *Cibicidoides wuellerstorfi* and *Uvigerina peregrina*, were picked at each 20 cm interval from the 250–355 mm size-fraction. All benthic foraminiferal δ^{18}O measurements were carried out at CEREGE using a mass spectrometer (Finnigan Delta Advantage) equipped with a carbonate preparation device. The measured isotopic values have been normalized against NBS19. Mean external reproducibility is better than 0.05‰. The *C. wuellerstorfi* δ^{18}O values were corrected by +0.64‰ to fit the *U. peregrina* d18O values (Shackleton, 1974). The glacial/interglacial amplitude of benthic foraminiferal δ^{18}O variations in core MD05-2930 (Fig. 2a) is very close to that of the benthic stack LR04. The chronology of the whole sediment sequence was obtained by correlating the MD05-2930 benthic foraminiferal δ^{18}O record with the LR04 reference benthic stack (Lisiecki and Raymo, 2005) (Fig. 2b). This correlation places the MD05-2930 core bottom

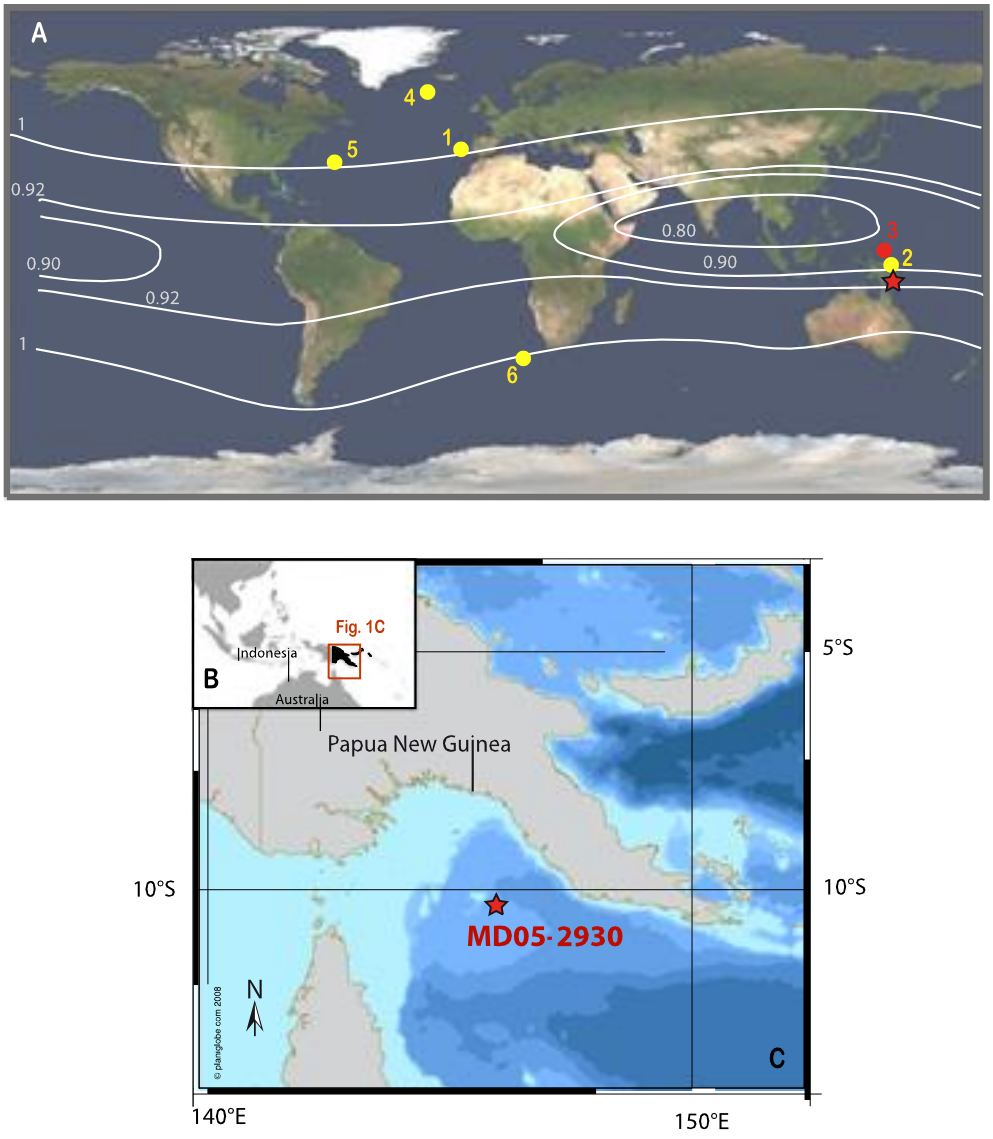

Fig. 1. (A) Location of the studied site among several recently published $^{10}Be/^{9}Be$ and $^{10}Be/^{230}Th_{xs}$ high-resolution marine records spanning the past ~ 300 ka (yellow) and older (red). 1: Carcaillet et al. (2004b); Ménabréaz et al. (2011). 2: Ménabréaz et al. (2012). 3: Carcaillet et al. (2003). 4, 5: Christl et al. (2010); Knudsen et al. (2008). 6: Christl et al. (2007). The star represents the location of core MD05-2930. (B) precise core location and (C) bathymetry of the Gulf of Papua. The contour lines represent the lines of equal intensity of cosmic rays at sea level (after Legrand, 1984). (For interpretation of the references to colour in this figure, the reader is referred to the web version of this article.)

(3670 cm depth) in Marine Isotope Stage (MIS) 20. This is in agreement with the identification of a paleomagnetic reversal recorded at 3610 cm in MIS 19, corresponding to the Brunhes–Matuyama (B/M) polarity transition (Thouveny et al., in preparation) dated between 773 and 781 ka by absolute datings on lava flows (e.g. Singer and Pringle, 1996; Quidelleur et al., 2003) or by astronomical tuning of sediment sequences (e.g. Bassinot et al., 1994; Tauxe et al., 1996; Channell et al., 2010). According to these chronological constraints, the average sedimentation rate of the MD05-2930 sedimentary sequence is about 4.6 cm/ka (Fig. 2c).

2.3. Sampling and chemical procedures for authigenic ^{10}Be and ^{9}Be extraction, and authigenic ^{10}Be and ^{9}Be measurements

The sampling of core MD05-2930 was performed from 1400 to 3670 cm depth, which corresponds to the 250–800 ka time interval (Fig. 2b). Since the upper part of core MD05-2930 is affected by artefacts due to piston coring, the last 250 ka are presently studied on core MD05-2920, collected on the Northern Papua margin (see Ménabréaz et al., 2012 for the 20–50 ka time interval). Sediment slices measuring 1cm thick were extracted every 10 cm besides u-channels collected for paleomagnetic sampling and X-ray fluorescence measurements. A total of 224 sediment samples were taken and were chemically treated to extract and analyse Beryllium isotopes in their authigenic phase.

All samples were processed for the Be isotopes analysis at the CEREGE National Cosmogenic Nuclides Laboratory, France. Already summarized by Carcaillet et al. (2003, 2004a, 2004b) and Ménabréaz et al. (2011, 2012), the chemical procedure is detailed below. Several procedural blanks and replicates were performed along with the samples in order to assess both cleanliness and reproducibility during the chemical extraction.

^{10}Be and its stable isotope ^{9}Be were co-extracted with the authigenic phase of sediments using 20 ml/$g_{sediment}$ of 0.04M hydroxylamine (NH_2OH-HCl) in a 25% acetic acid leaching solution at $(95 \pm 5)^{\circ}C$ for 7 hr (Bourlès et al., 1989). A 2 ml aliquot of the resulting leaching solution was taken for flameless Atomic Absorption Spectrophotometry (AAS) measurement of the natural ^{9}Be

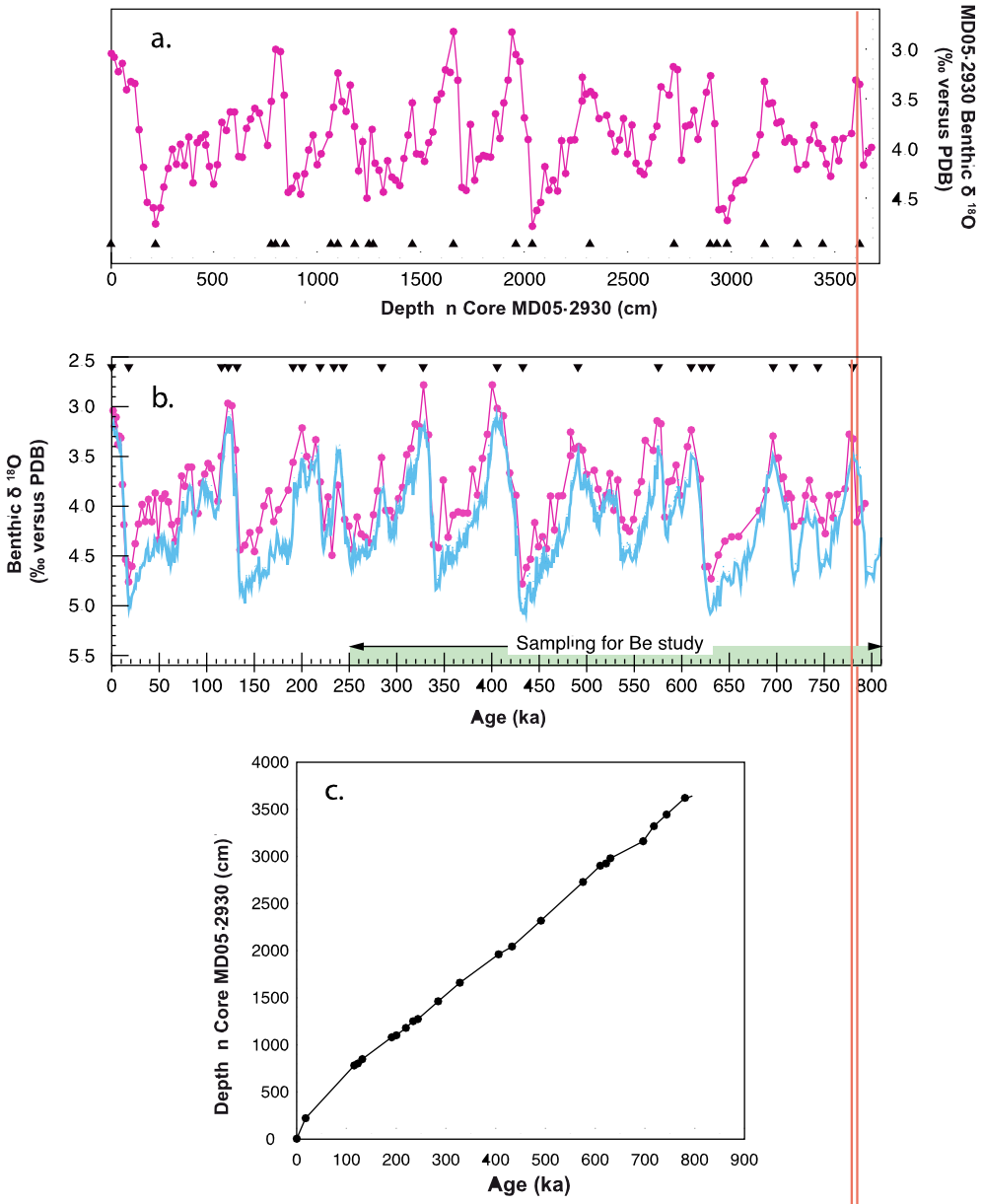

Fig. 2. Stable isotopes record of core MD05-2930 used for the time scale reconstruction: (a) benthic foraminifera *C. Wuellerstorfi* and *Uvigerina sp.* $\delta^{18}O$ records on the depth scale; black triangles locate the tie-points used for the correlation with the reference record LR04 of Lisiecki and Raymo (2005). (b) Benthic $\delta^{18}O$ record (pink) on the time scale established by correlation with the dated benthic stack LR04 (blue); black triangles locate the correlation tie points. The green bar indicates the interval 250–800 ka sampled for the Be isotopes analysis. (c) depth-age relationship used to transfer all studied parameters to the time scale. The red vertical line situates the stratigraphic position of the Brunhes–Matuyama reversal (see text). (For interpretation of the references to colour in this figure, the reader is referred to the web version of this article.)

concentration. The remaining solution was spiked with 300 μl of a 10^{-3} g/g ^{9}Be-carrier before the chemical extraction that was to be performed prior to the AMS measurement of the resulting $^{10}Be/^{9}Be$ ratio. The spiked solution was then evaporated to dryness the residues dissolved in HNO_3 and diluted with distilled water. The thus-solubilised Beryllium was then chelated at pH 7 by adding 2 ml of acetylacetone in the presence of EDTA 50%. The obtained Be-acetylacetonates were separated by organic solvent extraction using CCl_4, and heat decomposed in HCl. The solid residues resulting from the evaporation of the HCl – acidified extracted organic fraction were dissolved in a 4 ml HNO_3 – 2 ml $HClO_4$ acidic solution that was brought to dryness. The obtained residues were dissolved in ultra-pure HNO_3, the resulting solution was again evaporated to dryness and the solid residues were finally dissolved in ultra-pure HCl. Be oxy-hydroxides were precipitated at pH 8 from this final solution by adding NH_4OH. The precipitate was separated by centrifugation and rinsed twice by re-suspension and centrifugation in pH 8 ultra-pure water. After dissolution of this rinsed precipitate in HCl, the previously described precipitation and rinse steps were repeated. These purified Beryllium oxy-hydroxides were solubilised in HNO_3 and the resulting solution was transferred into a quartz crucible where it was gently evaporated to dryness at 200 °C. Finally, the Beryllium oxy-hydroxides deposit was fully converted to BeO by oven heating at 800 °C for 1 hr in order to condition it for AMS measurements.

^{10}Be concentration measurements were performed at the French AMS national facility ASTER (CEREGE) operating at 5MV. Once an aliquot is taken for natural authigenic ^{9}Be measurements, the addition of an accurately and precisely known concentration of ^{9}Be-carrier to the leaching solutions before any chemical handling allows to accurately determine ^{10}Be sample concentrations from the measured $^{10}Be/^{9}Be$ ratios, normalized to the

Table 1
AMS measurements, authigenic ^{10}Be and ^{9}Be concentrations, and authigenic $^{10}Be/^{9}Be$ ratios of core MD05-2930 samples.

Sample: depth in core MD05-2930 (cm)	Age (ka BP)	Sample weight (g)	Measured $^{10}Be/^{9}Be$ (10^{-11})*	$[^{10}Be]_{auth.}$ corrected from radioactive decay (10^{-15} g/g)*	Authigenic $[^{9}Be]$ (10^{-7} g/g)*	Authigenic $^{10}Be/^{9}Be$ (10^{-8})*
MD05-2930_1401	271	1.03	2.984 ± 0.043	9.43 ± 0.14	3.15 ± 0.07	2.99 ± 0.08
MD05-2930_1411	273	0.69	2.143 ± 0.020	10.09 ± 0.10	3.38 ± 0.06	2.98 ± 0.06
MD05-2930_1421	275	1.03	3.196 ± 0.022	10.21 ± 0.08	3.55 ± 0.07	2.87 ± 0.06
MD05-2930_1431	278	1.12	3.014 ± 0.048	8.93 ± 0.15	3.19 ± 0.19	2.80 ± 0.17
MD05-2930_1441	280	0.87	2.237 ± 0.021	8.51 ± 0.09	3.58 ± 0.06	2.37 ± 0.05
MD05-2930_1451	282	0.93	2.781 ± 0.020	9.78 ± 0.08	3.09 ± 0.05	3.16 ± 0.05
MD05-2930_1461	284	1.04	3.164 ± 0.051	10.27 ± 0.17	2.80 ± 0.19	3.68 ± 0.25
MD05-2930_1471	286	0.90	2.865 ± 0.029	10.65 ± 0.11	2.80 ± 0.07	3.81 ± 0.10
MD05-2930_1481	288	0.81	2.373 ± 0.018	9.93 ± 0.08	2.72 ± 0.04	3.65 ± 0.06
MD05-2930_1491	291	1.02	2.877 ± 0.044	9.47 ± 0.15	3.05 ± 0.14	3.11 ± 0.15
MD05-2930_1501	293	0.81	2.517 ± 0.019	10.48 ± 0.08	3.34 ± 0.02	3.14 ± 0.03
MD05-2930_1511	295	1.00	3.055 ± 0.023	10.27 ± 0.08	3.19 ± 0.05	3.22 ± 0.06
MD05-2930_1521	297	0.94	2.448 ± 0.039	8.63 ± 0.14	3.24 ± 0.20	2.66 ± 0.17
MD05-2930_1531	299	1.10	2.571 ± 0.019	7.83 ± 0.06	3.19 ± 0.03	2.45 ± 0.03
MD05-2930_1541	302	0.98	1.950 ± 0.019	6.70 ± 0.07	2.66 ± 0.03	2.52 ± 0.04
MD05-2930_1551	304	1.05	2.263 ± 0.040	7.20 ± 0.13	3.42 ± 0.08	2.11 ± 0.06
MD05-2930_1561	306	0.92	2.476 ± 0.024	8.89 ± 0.09	3.87 ± 0.04	2.30 ± 0.03
MD05-2930_1571	308	1.10	3.174 ± 0.022	9.17 ± 0.07	2.93 ± 0.06	3.13 ± 0.06
MD05-2930_1581	310	1.02	2.722 ± 0.043	8.96 ± 0.14	2.79 ± 0.05	3.20 ± 0.08
MD05-2930_1591	313	1.02	3.041 ± 0.021	9.92 ± 0.07	3.00 ± 0.06	3.31 ± 0.07
MD05-2930_1601	315	0.85	2.170 ± 0.016	8.63 ± 0.07	2.73 ± 0.09	3.16 ± 0.11
MD05-2930_1611	317	0.88	2.166 ± 0.033	8.25 ± 0.13	3.08 ± 0.11	2.68 ± 0.11
MD05-2930_1621	319	0.54	1.408 ± 0.013	8.83 ± 0.08	2.60 ± 0.05	3.40 ± 0.08
MD05-2930_1631	322	1.04	2.874 ± 0.022	9.33 ± 0.07	3.26 ± 0.08	2.86 ± 0.07
MD05-2930_1641	324	0.76	1.978 ± 0.055	8.70 ± 0.24	2.91 ± 0.11	2.99 ± 0.14
MD05-2930_1651	326	0.75	1.969 ± 0.016	8.78 ± 0.07	2.70 ± 0.06	3.25 ± 0.07
MD05-2930_1661	328	0.74	1.942 ± 0.019	8.68 ± 0.09	2.74 ± 0.04	3.16 ± 0.06
MD05-2930_1671	331	0.97	1.940 ± 0.054	6.70 ± 0.19	3.17 ± 0.08	2.11 ± 0.08
MD05-2930_1681	333	0.70	1.281 ± 0.014	6.11 ± 0.07	3.19 ± 0.05	1.92 ± 0.04
MD05-2930_1691	336	0.89	1.767 ± 0.015	6.59 ± 0.06	3.15 ± 0.04	2.09 ± 0.03
MD05-2930_1701	339	0.91	1.994 ± 0.074	7.24 ± 0.27	3.26 ± 0.08	2.22 ± 0.10
MD05-2930_1711	341	1.03	2.040 ± 0.021	6.65 ± 0.07	2.68 ± 0.04	2.49 ± 0.05
MD05-2930_1721	344	0.67	1.068 ± 0.015	5.14 ± 0.07	2.09 ± 0.07	2.47 ± 0.08
MD05-2930_1731	346	0.89	1.547 ± 0.073	5.80 ± 0.28	3.04 ± 0.06	1.91 ± 0.10
MD05-2930_1741	349	1.12	2.418 ± 0.017	6.87 ± 0.05	2.43 ± 0.07	2.83 ± 0.08
MD05-2930_1751	351	1.02	2.288 ± 0.019	7.51 ± 0.07	2.43 ± 0.07	3.09 ± 0.09
MD05-2930_1761	354	1.01	2.528 ± 0.057	8.26 ± 0.19	2.89 ± 0.10	2.85 ± 0.12
MD05-2930_1771	357	1.28	3.281 ± 0.020	8.64 ± 0.06	2.95 ± 0.02	2.93 ± 0.03
MD05-2930_1781	359	1.12	2.714 ± 0.022	8.15 ± 0.07	2.60 ± 0.01	3.13 ± 0.03
MD05-2930_1791	362	0.81	1.828 ± 0.061	7.45 ± 0.25	3.06 ± 0.04	2.44 ± 0.09
MD05-2930_1801	364	0.77	1.819 ± 0.016	8.02 ± 0.07	3.09 ± 0.09	2.59 ± 0.08
MD05-2930_1811	367	0.98	2.512 ± 0.015	8.50 ± 0.05	2.48 ± 0.05	3.43 ± 0.07
MD05-2930_1821	370	1.00	2.585 ± 0.046	8.64 ± 0.16	3.24 ± 0.10	2.67 ± 0.09
MD05-2930_1831	372	1.15	3.252 ± 0.021	9.41 ± 0.06	2.85 ± 0.05	3.30 ± 0.06
MD05-2930_1841	375	1.25	3.451 ± 0.021	9.25 ± 0.06	3.14 ± 0.06	2.95 ± 0.06
MD05-2930_1851	377	1.11	3.180 ± 0.051	9.58 ± 0.16	3.27 ± 0.09	2.93 ± 0.09
MD05-2930_1861	380	1.19	3.482 ± 0.022	9.80 ± 0.06	2.92 ± 0.05	3.36 ± 0.06
MD05-2930_1871	382	1.30	3.401 ± 0.028	8.73 ± 0.07	3.31 ± 0.07	2.64 ± 0.06
MD05-2930_1881	385	0.92	2.460 ± 0.043	8.93 ± 0.16	4.18 ± 0.04	2.14 ± 0.05
MD05-2930_1891	388	0.86	2.091 ± 0.018	8.13 ± 0.07	3.03 ± 0.03	2.69 ± 0.04
MD05-2930_1901	390	1.13	3.292 ± 0.020	9.77 ± 0.06	3.59 ± 0.14	2.72 ± 0.10
MD05-2930_1911	393	0.95	2.579 ± 0.054	9.07 ± 0.19	3.30 ± 0.13	2.75 ± 0.11
MD05-2930_1921	395	0.79	2.111 ± 0.017	8.90 ± 0.07	2.79 ± 0.08	3.20 ± 0.09
MD05-2930_1931	398	0.90	2.308 ± 0.020	8.54 ± 0.08	2.72 ± 0.06	3.14 ± 0.08
MD05-2930_1941	401	1.02	2.347 ± 0.043	7.65 ± 0.14	2.3751 ± 0.0002	3.22 ± 0.06
MD05-2930_1951	403	0.99	2.600 ± 0.017	8.76 ± 0.06	2.48 ± 0.07	3.54 ± 0.11
MD05-2930_1961	406	0.82	2.275 ± 0.017	9.10 ± 0.07	2.46 ± 0.08	3.70 ± 0.13
MD05-2930_1971	409	0.99	2.691 ± 0.057	9.06 ± 0.20	3.05 ± 0.04	2.97 ± 0.07
MD05-2930_1981	412	0.99	2.683 ± 0.018	9.14 ± 0.06	2.54 ± 0.08	3.60 ± 0.12
MD05-2930_1991	416	1.21	2.849 ± 0.019	7.80 ± 0.06	3.04 ± 0.08	2.57 ± 0.07
MD05-2930_2001	419	1.05	2.169 ± 0.026	6.86 ± 0.08	2.83 ± 0.08	2.43 ± 0.08
MD05-2930_2011	422	1.25	2.547 ± 0.018	6.80 ± 0.05	2.77 ± 0.08	2.45 ± 0.07
MD05-2930_2021	425	1.23	2.468 ± 0.017	6.73 ± 0.05	2.70 ± 0.09	2.49 ± 0.08
MD05-2930_2041	432	1.05	2.464 ± 0.022	7.86 ± 0.07	2.50 ± 0.03	3.14 ± 0.04
MD05-2930_2051	434	1.16	3.197 ± 0.021	9.27 ± 0.07	2.96 ± 0.13	3.13 ± 0.14
MD05-2930_2061	437	1.06	3.049 ± 0.029	9.49 ± 0.09	3.04 ± 0.06	3.12 ± 0.06
MD05-2930_2071	439	1.20	3.401 ± 0.026	9.49 ± 0.07	2.94 ± 0.04	3.23 ± 0.15
MD05-2930_2081	441	1.02	2.034 ± 0.018	6.68 ± 0.06	2.56 ± 0.05	2.60 ± 0.05
MD05-2930_2091	443	0.62	1.137 ± 0.022	6.10 ± 0.12	2.51 ± 0.08	2.43 ± 0.09
MD05-2930_2101	445	1.07	2.334 ± 0.022	7.34 ± 0.07	2.39 ± 0.11	3.06 ± 0.14
MD05-2930_2111	447	1.07	2.901 ± 0.019	9.02 ± 0.06	2.66 ± 0.02	3.38 ± 0.03
MD05-2930_2121	449	1.21	3.462 ± 0.039	9.58 ± 0.11	3.11 ± 0.03	3.08 ± 0.05

Table 1 (*continued*)

Sample: depth in core MD05-2930 (cm)	Age (ka BP)	Sample weight (g)	Measured $^{10}Be/^{9}Be$ (10^{-11})*	$[^{10}Be]_{auth.}$ corrected from radioactive decay (10^{-15} g/g)*	Authigenic $[^{9}Be]$ (10^{-7} g/g)*	Authigenic $^{10}Be/^{9}Be$ (10^{-8})*
MD05-2930_2131	451	1.18	3.052 ± 0.024	8.73 ± 0.07	2.80 ± 0.03	3.12 ± 0.04
MD05-2930_2141	453	0.95	2.356 ± 0.019	8.33 ± 0.07	2.84 ± 0.02	2.93 ± 0.03
MD05-2930_2151	455	0.98	1.594 ± 0.027	5.43 ± 0.10	3.18 ± 0.06	1.71 ± 0.04
MD05-2930_2161	458	0.91	1.906 ± 0.015	7.02 ± 0.06	3.16 ± 0.04	2.22 ± 0.04
MD05-2930_2181	462	0.79	2.257 ± 0.025	9.47 ± 0.11	4.15 ± 0.08	2.28 ± 0.05
MD05-2930_2191	464	0.86	1.824 ± 0.014	7.11 ± 0.06	4.22 ± 0.04	1.68 ± 0.02
MD05-2930_2201	466	1.09	2.737 ± 0.018	8.28 ± 0.06	4.07 ± 0.09	2.03 ± 0.05
MD05-2930_2211	468	0.99	2.593 ± 0.021	8.71 ± 0.07	4.48 ± 0.04	1.94 ± 0.03
MD05-2930_2221	470	1.21	3.001 ± 0.024	8.36 ± 0.07	3.58 ± 0.06	2.34 ± 0.04
MD05-2930_2231	472	1.06	2.588 ± 0.020	8.14 ± 0.07	4.17 ± 0.09	1.95 ± 0.05
MD05-2930_2241	474	1.11	2.428 ± 0.036	7.33 ± 0.11	4.19 ± 0.10	1.75 ± 0.05
MD05-2930_2251	477	1.16	2.252 ± 0.017	6.49 ± 0.05	3.59 ± 0.04	1.81 ± 0.03
MD05-2930_2261	479	0.89	1.801 ± 0.032	6.67 ± 0.12	4.10 ± 0.06	1.63 ± 0.04
MD05-2930_2271	481	0.85	1.295 ± 0.023	5.11 ± 0.10	4.29 ± 0.13	1.19 ± 0.05
MD05-2930_2281	483	0.86	0.664 ± 0.008	2.61 ± 0.04	2.22 ± 0.01	1.18 ± 0.02
MD05-2930_2291	485	1.01	1.867 ± 0.021	6.22 ± 0.07	3.78 ± 0.09	1.64 ± 0.05
MD05-2930_2301	487	1.04	1.948 ± 0.037	6.27 ± 0.12	2.62 ± 0.04	2.39 ± 0.06
MD05-2930_2311	489	1.05	2.215 ± 0.016	7.18 ± 0.05	2.79 ± 0.02	2.58 ± 0.03
MD05-2930_2321	491	0.96	2.416 ± 0.018	8.40 ± 0.06	3.06 ± 0.06	2.75 ± 0.06
MD05-2930_2331	493	1.16	3.052 ± 0.043	8.79 ± 0.13	3.64 ± 0.02	2.42 ± 0.04
MD05-2930_2341	495	1.12	2.864 ± 0.023	8.65 ± 0.07	3.32 ± 0.06	2.61 ± 0.05
MD05-2930_2351	498	1.14	2.920 ± 0.029	8.59 ± 0.09	3.26 ± 0.04	2.63 ± 0.04
MD05-2930_2361	500	0.87	2.059 ± 0.040	7.87 ± 0.16	3.51 ± 0.16	2.24 ± 0.11
MD05-2930_2371	502	0.75	1.652 ± 0.014	7.42 ± 0.06	3.19 ± 0.02	2.33 ± 0.03
MD05-2930_2381	504	0.96	2.014 ± 0.015	7.04 ± 0.05	2.96 ± 0.03	2.38 ± 0.03
MD05-2930_2391	506	0.51	1.046 ± 0.012	6.89 ± 0.08	2.91 ± 0.15	2.37 ± 0.13
MD05-2930_2401	508	0.94	1.949 ± 0.016	6.98 ± 0.06	2.91 ± 0.03	2.40 ± 0.03
MD05-2930_2411	510	0.95	1.966 ± 0.016	6.89 ± 0.06	2.97 ± 0.04	2.32 ± 0.04
MD05-2930_2421	512	0.73	1.516 ± 0.018	6.95 ± 0.08	3.30 ± 0.08	2.11 ± 0.06
MD05-2930_2431	514	0.84	1.705 ± 0.014	6.77 ± 0.06	3.18 ± 0.04	2.13 ± 0.04
MD05-2930_2441	516	0.97	1.871 ± 0.018	6.49 ± 0.07	2.97 ± 0.01	2.18 ± 0.03
MD05-2930_2451	518	0.45	0.991 ± 0.012	7.37 ± 0.09	3.58 ± 0.17	2.06 ± 0.10
MD05-2930_2461	520	0.86	2.182 ± 0.017	8.50 ± 0.07	2.97 ± 0.03	2.86 ± 0.04
MD05-2930_2471	522	0.94	2.360 ± 0.020	8.43 ± 0.07	2.84 ± 0.05	2.97 ± 0.06
MD05-2930_2481	524	0.58	1.567 ± 0.018	9.04 ± 0.10	3.23 ± 0.09	2.80 ± 0.09
MD05-2930_2491	526	1.11	3.106 ± 0.022	9.44 ± 0.07	3.00 ± 0.10	3.14 ± 0.11
MD05-2930_2501	529	1.06	2.813 ± 0.023	8.95 ± 0.08	3.09 ± 0.03	2.90 ± 0.04
MD05-2930_2511	531	0.72	1.767 ± 0.021	8.19 ± 0.10	3.57 ± 0.03	2.29 ± 0.03
MD05-2930_2521	533	0.83	1.949 ± 0.014	7.91 ± 0.06	2.97 ± 0.08	2.66 ± 0.08
MD05-2930_2531	535	1.09	3.295 ± 0.019	10.13 ± 0.06	3.48 ± 0.07	2.91 ± 0.06
MD05-2930_2541	537	0.60	2.054 ± 0.022	11.53 ± 0.12	3.07 ± 0.12	3.76 ± 0.16
MD05-2930_2551	539	1.00	3.640 ± 0.022	12.31 ± 0.08	3.22 ± 0.11	3.82 ± 0.13
MD05-2930_2561	541	1.10	3.857 ± 0.027	11.91 ± 0.09	3.06 ± 0.09	3.88 ± 0.11
MD05-2930_2571	543	0.53	1.686 ± 0.018	10.70 ± 0.12	3.40 ± 0.04	3.15 ± 0.13
MD05-2930_2581	545	1.18	3.202 ± 0.018	9.14 ± 0.06	3.71 ± 0.13	2.46 ± 0.09
MD05-2930_2591	547	0.78	1.988 ± 0.015	8.64 ± 0.07	3.42 ± 0.07	2.53 ± 0.05
MD05-2930_2601	549	0.60	1.596 ± 0.020	8.92 ± 0.11	3.71 ± 0.04	2.40 ± 0.10
MD05-2930_2611	551	0.85	2.341 ± 0.018	9.22 ± 0.07	3.10 ± 0.08	2.97 ± 0.08
MD05-2930_2621	553	0.97	2.787 ± 0.018	9.11 ± 0.06	3.70 ± 0.05	2.46 ± 0.04
MD05-2930_2631	555	0.83	1.956 ± 0.022	7.77 ± 0.09	3.73 ± 0.06	2.08 ± 0.04
MD05-2930_2641	557	0.88	2.016 ± 0.014	7.72 ± 0.06	3.58 ± 0.13	2.16 ± 0.08
MD05-2930_2651	559	1.06	2.264 ± 0.019	7.19 ± 0.06	4.06 ± 0.03	1.77 ± 0.02
MD05-2930_2661	562	0.75	1.586 ± 0.018	7.07 ± 0.08	3.82 ± 0.08	1.85 ± 0.05
MD05-2930_2671	564	1.11	2.519 ± 0.017	7.62 ± 0.05	4.36 ± 0.16	1.75 ± 0.07
MD05-2930_2681	566	0.81	1.745 ± 0.016	7.20 ± 0.07	3.68 ± 0.13	1.96 ± 0.07
MD05-2930_2691	568	0.79	1.760 ± 0.019	6.97 ± 0.08	3.43 ± 0.09	2.03 ± 0.06
MD05-2930_2701	570	0.88	1.934 ± 0.016	7.27 ± 0.06	2.56 ± 0.05	2.83 ± 0.06
MD05-2930_2711	572	0.73	1.540 ± 0.015	7.13 ± 0.07	2.87 ± 0.06	2.49 ± 0.06
MD05-2930_2721	574	0.59	1.306 ± 0.015	7.28 ± 0.09	2.80 ± 0.11	2.60 ± 0.11
MD05-2930_2731	576	0.88	1.904 ± 0.028	7.22 ± 0.11	2.48 ± 0.06	2.91 ± 0.08
MD05-2930_2741	578	1.10	2.426 ± 0.027	7.39 ± 0.09	2.48 ± 0.18	2.98 ± 0.22
MD05-2930_2751	580	0.76	1.869 ± 0.021	8.34 ± 0.09	3.47 ± 0.10	2.40 ± 0.08
MD05-2930_2761	582	1.10	3.343 ± 0.037	10.21 ± 0.12	3.49 ± 0.07	2.93 ± 0.07
MD05-2930_2771	584	1.10	3.871 ± 0.042	11.80 ± 0.13	4.08 ± 0.08	2.89 ± 0.06
MD05-2930_2781	586	0.99	3.547 ± 0.039	11.94 ± 0.13	3.33 ± 0.10	3.58 ± 0.12
MD05-2930_2791	588	1.06	3.334 ± 0.041	10.56 ± 0.13	3.90 ± 0.07	2.71 ± 0.06
MD05-2930_2801	590	0.86	2.355 ± 0.032	9.21 ± 0.13	3.20 ± 0.12	2.87 ± 0.11
MD05-2930_2811	592	0.68	1.566 ± 0.017	7.67 ± 0.09	3.59 ± 0.08	2.14 ± 0.05
MD05-2930_2821	594	0.80	1.597 ± 0.025	6.67 ± 0.11	3.09 ± 0.08	2.16 ± 0.07
MD05-2930_2831	596	0.91	1.924 ± 0.023	7.10 ± 0.09	3.13 ± 0.07	2.27 ± 0.06
MD05-2930_2841	598	0.86	1.819 ± 0.021	7.09 ± 0.08	3.54 ± 0.08	2.01 ± 0.05
MD05-2930_2851	600	0.90	2.059 ± 0.029	7.64 ± 0.11	3.57 ± 0.02	2.14 ± 0.04
MD05-2930_2861	602	1.08	2.422 ± 0.027	7.47 ± 0.09	3.76 ± 0.03	1.99 ± 0.03

(*continued on next page*)

Table 1 (*continued*)

Sample: depth in core MD05-2930 (cm)	Age (ka BP)	Sample weight (g)	Measured $^{10}Be/^{9}Be$ (10^{-11})*	$[^{10}Be]_{auth.}$ corrected from radioactive decay (10^{-15} g/g)*	Authigenic $[^{9}Be]$ (10^{-7} g/g)*	Authigenic $^{10}Be/^{9}Be$ (10^{-8})*
MD05-2930_2871	604	0.51	1.241 ± 0.010	8.17 ± 0.06	4.05 ± 0.15	2.02 ± 0.08
MD05-2930_2881	606	0.73	1.843 ± 0.029	8.37 ± 0.13	3.45 ± 0.03	2.43 ± 0.05
MD05-2930_2891	608	0.78	1.771 ± 0.029	7.46 ± 0.13	2.85 ± 0.03	2.61 ± 0.06
MD05-2930_2911	615	0.98	2.722 ± 0.031	9.26 ± 0.11	2.96 ± 0.08	3.13 ± 0.09
MD05-2930_2921	620	0.82	1.957 ± 0.026	8.03 ± 0.11	3.04 ± 0.08	2.64 ± 0.08
MD05-2930_2931	623	0.60	1.346 ± 0.011	7.42 ± 0.06	2.92 ± 0.10	2.54 ± 0.09
MD05-2930_2941	624	1.21	2.948 ± 0.037	8.15 ± 0.11	2.92 ± 0.01	2.79 ± 0.04
MD05-2930_2951	626	1.29	3.189 ± 0.041	8.30 ± 0.11	3.35 ± 0.08	2.48 ± 0.07
MD05-2930_2961	627	0.57	1.229 ± 0.010	7.14 ± 0.06	3.21 ± 0.03	2.23 ± 0.03
MD05-2930_2971	629	0.83	1.324 ± 0.025	5.33 ± 0.10	3.03 ± 0.10	1.76 ± 0.07
MD05-2930_2981	631	0.92	1.500 ± 0.027	5.42 ± 0.09	3.20 ± 0.12	1.69 ± 0.07
MD05-2930_2991	634	0.66	1.171 ± 0.013	5.80 ± 0.06	3.07 ± 0.08	1.89 ± 0.05
MD05-2930_3001	638	1.18	2.075 ± 0.028	5.88 ± 0.08	2.77 ± 0.05	2.12 ± 0.05
MD05-2930_3011	642	1.25	2.347 ± 0.025	5.93 ± 0.07	3.13 ± 0.06	1.90 ± 0.04
MD05-2930_3021	645	0.74	1.257 ± 0.013	5.60 ± 0.06	2.88 ± 0.03	1.95 ± 0.03
MD05-2930_3031	649	0.91	1.590 ± 0.019	5.78 ± 0.07	2.85 ± 0.01	2.03 ± 0.03
MD05-2930_3041	653	0.97	1.686 ± 0.020	5.76 ± 0.07	2.93 ± 0.04	1.97 ± 0.04
MD05-2930_3051	656	0.74	0.999 ± 0.011	4.50 ± 0.05	2.34 ± 0.10	1.93 ± 0.08
MD05-2930_3071	663	1.02	1.805 ± 0.012	5.90 ± 0.07	3.46 ± 0.08	1.70 ± 0.05
MD05-2930_3081	667	0.53	0.874 ± 0.011	5.35 ± 0.06	2.94 ± 0.09	1.82 ± 0.06
MD05-2930_3091	671	0.92	1.654 ± 0.012	6.03 ± 0.07	2.77 ± 0.10	2.18 ± 0.08
MD05-2930_3101	674	1.28	2.053 ± 0.014	5.38 ± 0.08	2.52 ± 0.06	2.14 ± 0.06
MD05-2930_3111	678	0.65	1.447 ± 0.010	7.38 ± 0.08	3.23 ± 0.10	2.28 ± 0.08
MD05-2930_3121	682	0.52	1.279 ± 0.014	8.21 ± 0.12	3.43 ± 0.17	2.39 ± 0.12
MD05-2930_3131	685	1.02	2.684 ± 0.020	8.85 ± 0.18	3.63 ± 0.04	2.44 ± 0.06
MD05-2930_3141	688	0.95	2.497 ± 0.009	8.86 ± 0.08	4.28 ± 0.12	2.07 ± 0.06
MD05-2930_3151	692	0.74	1.877 ± 0.009	8.44 ± 0.08	3.32 ± 0.06	2.54 ± 0.05
MD05-2930_3161	696	1.02	2.443 ± 0.011	8.11 ± 0.09	3.46 ± 0.08	2.35 ± 0.06
MD05-2930_3171	698	0.88	1.769 ± 0.012	6.80 ± 0.08	3.14 ± 0.02	2.16 ± 0.03
MD05-2930_3181	699	0.66	1.303 ± 0.011	6.70 ± 0.08	2.65 ± 0.11	2.53 ± 0.11
MD05-2930_3191	700	0.84	1.721 ± 0.013	6.91 ± 0.09	2.33 ± 0.05	2.97 ± 0.07
MD05-2930_3201	702	0.93	1.975 ± 0.012	7.12 ± 0.09	3.04 ± 0.06	2.34 ± 0.05
MD05-2930_3211	703	0.83	1.654 ± 0.009	6.69 ± 0.06	2.65 ± 0.08	2.53 ± 0.08
MD05-2930_3221	704	0.94	1.779 ± 0.012	6.39 ± 0.08	2.54 ± 0.02	2.52 ± 0.04
MD05-2930_3231	706	1.23	2.533 ± 0.009	6.93 ± 0.07	3.49 ± 0.05	1.99 ± 0.03
MD05-2930_3241	707	0.58	1.126 ± 0.014	6.59 ± 0.09	3.25 ± 0.09	2.03 ± 0.07
MD05-2930_3251	708	1.09	1.782 ± 0.012	5.50 ± 0.07	3.28 ± 0.08	1.68 ± 0.05
MD05-2930_3261	710	1.16	2.152 ± 0.011	6.28 ± 0.07	3.81 ± 0.08	1.65 ± 0.04
MD05-2930_3271	711	0.50	0.917 ± 0.012	6.13 ± 0.07	3.45 ± 0.03	1.78 ± 0.03
MD05-2930_3281	712	1.08	1.957 ± 0.012	6.14 ± 0.08	3.46 ± 0.06	1.77 ± 0.04
MD05-2930_3291	714	1.23	2.497 ± 0.012	6.78 ± 0.08	3.12 ± 0.06	2.17 ± 0.05
MD05-2930_3301	715	0.60	1.239 ± 0.013	7.09 ± 0.10	2.81 ± 0.11	2.53 ± 0.11
MD05-2930_3311	716	0.99	1.879 ± 0.008	6.27 ± 0.05	2.70 ± 0.04	2.32 ± 0.04
MD05-2930_3321	718	0.73	1.330 ± 0.011	6.09 ± 0.07	2.91 ± 0.10	2.10 ± 0.08
MD05-2930_3331	720	0.51	0.897 ± 0.012	5.90 ± 0.07	2.88 ± 0.05	2.05 ± 0.05
MD05-2930_3341	722	0.87	1.657 ± 0.010	6.36 ± 0.07	3.02 ± 0.06	2.11 ± 0.05
MD05-2930_3351	724	0.99	1.723 ± 0.012	5.85 ± 0.07	2.91 ± 0.08	2.01 ± 0.06
MD05-2930_3361	726	0.71	1.211 ± 0.013	5.76 ± 0.07	2.84 ± 0.11	2.03 ± 0.09
MD05-2930_3371	728	0.90	1.481 ± 0.011	5.52 ± 0.06	3.54 ± 0.06	1.56 ± 0.03
MD05-2930_3381	730	0.85	1.465 ± 0.012	5.73 ± 0.07	4.20 ± 0.06	1.37 ± 0.03
MD05-2930_3391	732	0.69	1.163 ± 0.011	5.69 ± 0.07	3.19 ± 0.04	1.79 ± 0.03
MD05-2930_3401	734	0.86	1.479 ± 0.010	5.77 ± 0.06	3.54 ± 0.06	1.63 ± 0.03
MD05-2930_3411	736	0.88	1.391 ± 0.011	5.34 ± 0.06	2.64 ± 0.04	2.02 ± 0.04
MD05-2930_3421	738	0.67	1.103 ± 0.016	5.56 ± 0.09	3.01 ± 0.06	1.85 ± 0.05
MD05-2930_3431	741	0.88	1.458 ± 0.012	5.59 ± 0.07	3.13 ± 0.07	1.79 ± 0.05
MD05-2930_3441	743	0.81	1.276 ± 0.013	5.33 ± 0.07	3.01 ± 0.07	1.77 ± 0.05
MD05-2930_3451	745	0.68	1.022 ± 0.013	5.05 ± 0.07	2.60 ± 0.02	1.94 ± 0.03
MD05-2930_3461	747	0.77	1.058 ± 0.013	4.63 ± 0.06	2.78 ± 0.02	1.67 ± 0.03
MD05-2930_3471	749	0.86	1.320 ± 0.014	5.10 ± 0.07	2.77 ± 0.06	1.84 ± 0.05
MD05-2930_3481	751	0.94	1.497 ± 0.009	5.36 ± 0.05	2.83 ± 0.03	1.90 ± 0.03
MD05-2930_3491	753	0.96	1.458 ± 0.010	5.10 ± 0.05	3.11 ± 0.07	1.64 ± 0.04
MD05-2930_3501	755	0.79	1.298 ± 0.012	5.44 ± 0.07	2.91 ± 0.03	1.87 ± 0.03
MD05-2930_3511	757	0.80	1.212 ± 0.018	4.99 ± 0.09	2.95 ± 0.05	1.69 ± 0.04
MD05-2930_3521	759	0.82	1.255 ± 0.013	5.13 ± 0.07	2.82 ± 0.03	1.82 ± 0.03
MD05-2930_3531	761	0.86	1.555 ± 0.010	6.05 ± 0.06	2.29 ± 0.03	2.63 ± 0.04
MD05-2930_3541	763	1.08	2.304 ± 0.010	7.11 ± 0.07	3.06 ± 0.07	2.32 ± 0.06
MD05-2930_3551	766	1.03	2.501 ± 0.009	8.12 ± 0.07	3.00 ± 0.03	2.70 ± 0.04
MD05-2930_3561	768	0.81	2.369 ± 0.009	9.78 ± 0.09	2.57 ± 0.06	3.81 ± 0.09
MD05-2930_3571	770	0.71	2.350 ± 0.009	11.01 ± 0.09	3.08 ± 0.05	3.58 ± 0.07
MD05-2930_3581	772	0.88	3.103 ± 0.008	11.71 ± 0.09	2.74 ± 0.07	4.28 ± 0.10
MD05-2930_3591	774	0.85	2.684 ± 0.009	10.57 ± 0.09	3.03 ± 0.05	3.48 ± 0.06
MD05-2930_3601	776	1.01	2.451 ± 0.009	8.17 ± 0.07	2.47 ± 0.05	3.32 ± 0.07
MD05-2930_3611	778	0.69	1.340 ± 0.013	6.56 ± 0.09	2.53 ± 0.04	2.60 ± 0.05

Table 1 (*continued*)

Sample: depth in core MD05-2930 (cm)	Age (ka BP)	Sample weight (g)	Measured $^{10}Be/^{9}Be$ (10^{-11})*	$[^{10}Be]_{auth.}$ corrected from radioactive decay (10^{-15} g/g)*	Authigenic $[^{9}Be]$ (10^{-7} g/g)*	Authigenic $^{10}Be/^{9}Be$ (10^{-8})*
MD05-2930_3621	780	0.78	1.400 ± 0.011	6.00 ± 0.07	2.53 ± 0.03	2.37 ± 0.04
MD05-2930_3631	782	1.05	1.794 ± 0.010	5.71 ± 0.06	2.60 ± 0.12	2.20 ± 0.10
MD05-2930_3641	784	0.61	1.074 ± 0.013	5.88 ± 0.06	2.94 ± 0.09	2.00 ± 0.07
MD05-2930_3651	786	0.57	1.130 ± 0.011	6.65 ± 0.06	2.81 ± 0.04	2.37 ± 0.05
MD05-2930_3661	789	0.84	2.163 ± 0.009	8.50 ± 0.06	3.04 ± 0.08	2.80 ± 0.08
MD05-2930_3671	791	1.09	2.589 ± 0.008	7.98 ± 0.06	3.12 ± 0.04	2.56 ± 0.04
mean ± std. dev.				7.71 ± 1.65	3.12 ± 0.46	2.51 ± 0.58
mean ± SDOM				7.71 ± 0.11	3.12 ± 0.03	2.51 ± 0.04

* 1-sigma uncertainties rounded to the higher value.

NIST 4325 Standard Reference Material ($(2.79 \pm 0.03) \times 10^{-11}$; Nishiizumi et al., 2007). The measured ratios and their uncertainties are presented in Table 1. Chemistry blank ratios range from 5.01×10^{-15} to 4.82×10^{-14}, which is at least 3 orders of magnitude lower than the sample $^{10}Be/^{9}Be$ ratios. The precision (from statistical and instrumental uncertainties) of the measured $^{10}Be/^{9}Be$ ratios ranges from 0.5% to 4%. Decay-corrected ^{10}Be concentrations have been computed using the ^{10}Be half-life of 1.387 ± 0.012 Ma (Chmeleff et al., 2010; Korschinek et al., 2010).

^{9}Be concentrations were measured at the CEREGE National Cosmogenic Nuclides Laboratory, France, using a graphite-furnace Atomic Absorption Spectrophotometer (AAS) with a Zeeman effect background correction (Thermo Scientific ICE 3400). The standard-additions method was used to eliminate the matrix effects during the absorption and to allow measurements near the detection limit. ^{9}Be sample concentrations (Table 1) were determined from repeated absorbance measurements (4 times) performed on each of the four 200 µl aliquots of the sample solution, three of them being spiked with increasing amount of a Sharlau ^{9}Be-carrier diluted to 0.34×10^{-8} g/g using HNO_3 0.2%. Procedure blanks were, in addition, processed for each sample run. The standard deviation of repeated absorbance measurements for each aliquot must be less than 1% to be considered. ^{9}Be concentrations of the unspiked sample aliquot were measured in the 10^{-10} g/g range. After correcting for sample dilution, the authigenic ^{9}Be sample concentrations along core MD05-2930 cluster around 10^{-7} g/g (Table 1). Associated uncertainties (1σ) vary from 0.01 to 7%.

3. Results

The authigenic Be concentrations presented in Fig. 3 along with the $\delta^{18}O$ profile (Fig. 3a) on the depth scale show that the authigenic ^{9}Be concentrations vary from 2.09 to 4.48×10^{-7} g/g and that the authigenic ^{10}Be concentrations vary from 2.61 to 12.31×10^{-15} g/g (Fig. 3b, c). It should be noted that the authigenic ^{10}Be and ^{9}Be concentrations are most likely influenced by the sedimentary particles adsorption efficiency depending, in particular, on their chemical composition and grain size distribution. Thus, contrary to the $^{10}Be/^{9}Be$ ratio, some of the ^{10}Be and ^{9}Be concentration variations may theoretically be attributable to environmental effects. However, the authigenic ^{9}Be variability is approximately twice as low as that of authigenic ^{10}Be, and most of the resulting $^{10}Be/^{9}Be$ variability is thus carried by the authigenic ^{10}Be signal (Fig. 3d). Comparison of the authigenic $^{10}Be/^{9}Be$ profile with the $\delta^{18}O$ paleoclimate proxy does not show any strong similarity (Fig. 3), which could be interpreted as a clue for a dependence of the ^{10}Be sedimentary fluxes on the glacial/interglacial cycles alternation.

The authigenic $^{10}Be/^{9}Be$ ratios vary between 1.18 and 4.28×10^{-8}. The $^{10}Be/^{9}Be$ peaks are labelled from VIII to XXI, in accordance with the nomenclature introduced by Carcaillet et al. (2004a) for the authigenic $^{10}Be/^{9}Be$ ratio peak series of the Portuguese margin. All peaks recorded in core MD05-2930 represent 1.4 to 2 times the values of the framing depth intervals, and exceed the value defined by "mean $+1\sigma$", except for numbers XIII, XVI, XIX and XX. The average of the highest $^{10}Be/^{9}Be$ values (above "mean $+1\sigma$") is 3.37×10^{-8}, and corresponds to a doubling of the average of the lowest values (below "mean -1σ") (1.68×10^{-8}).

The most prominent $^{10}Be/^{9}Be$ ratio peak, recorded at 3550–3600 cm, documents a 1.7-fold increase compared to the average ratio (2.51×10^{-8}) calculated over the whole studied time interval. The second major feature, recorded at 2530–2570 cm, documents a 1.55-fold increase compared to the long-term mean value. All the $^{10}Be/^{9}Be$ enhancement factors are listed in Table 2.

4. Interpretation of the $^{10}Be/^{9}Be$ dataset on a chronological scale: Global character and implications for the cosmogenic nuclides production during the B/M reversal and early Brunhes excursions

After being transferred to a time scale (cf. Section 2.2), the series of $^{10}Be/^{9}Be$ ratio peaks can be correlated with the series of the Geomagnetic Dipole Lows (GDL) documented in the SINT-2000 (Valet et al., 2005) and PISO-1500 (Channell et al., 2009) paleomagnetic reference records (Fig. 4).

The general correspondence between these time series confirms that the $^{10}Be/^{9}Be$ ratio variations recorded between 250 and 800 ka reflect the variation of the global ^{10}Be atmospheric production rate modulated by the magnetospheric shielding created by the geomagnetic dipole field. The events of cosmogenic Be overproduction recorded between 250 and 800 ka undoubtedly correspond to the series of Geomagnetic Dipole Lows evidenced in the SINT-2000 and PISO-1500 stacks, that are generally associated to paleomagnetic excursions (e.g. Channell et al., 2012) or to the Brunhes/Matuyama reversal (Table 2).

- Between 280 and 290 ka, interval VIII documents a significant (1.5-fold) increase of the ^{10}Be global production rate (Table 2) correlated with GDL g in both SINT-2000 and PISO-1500. GDL g was also reported at ~ 290 ka as an RPI low, inducing a ^{10}Be enhancement associated with the *Portuguese Margin* excursion (Thouveny et al., 2004; Carcaillet et al., 2004a). The new results presented herein are the first confirmation at low latitude of the occurrence of a global ^{10}Be overproduction at ~ 290 ka.
- Interval IX documents at ~ 313 and ~ 326 ka two events (~ 1.3-fold increases) of enhanced ^{10}Be global production rate corresponding to GDL h characterized by a double VDM minimum in PISO-1500. GDL h is associated with excursions reported at 310–330 ka (Langereis et al., 1997; Lund et al., 2001; Channell et al., 2012).
- Interval X documents several rapid and significant ^{10}Be overproduction events (~ 1.2- to ~ 1.3-fold increases) between 350 and 380 ka (Fig. 4). Between 395 and 415 ka, interval XI documents a ^{10}Be overproduction event centred at 406 ka

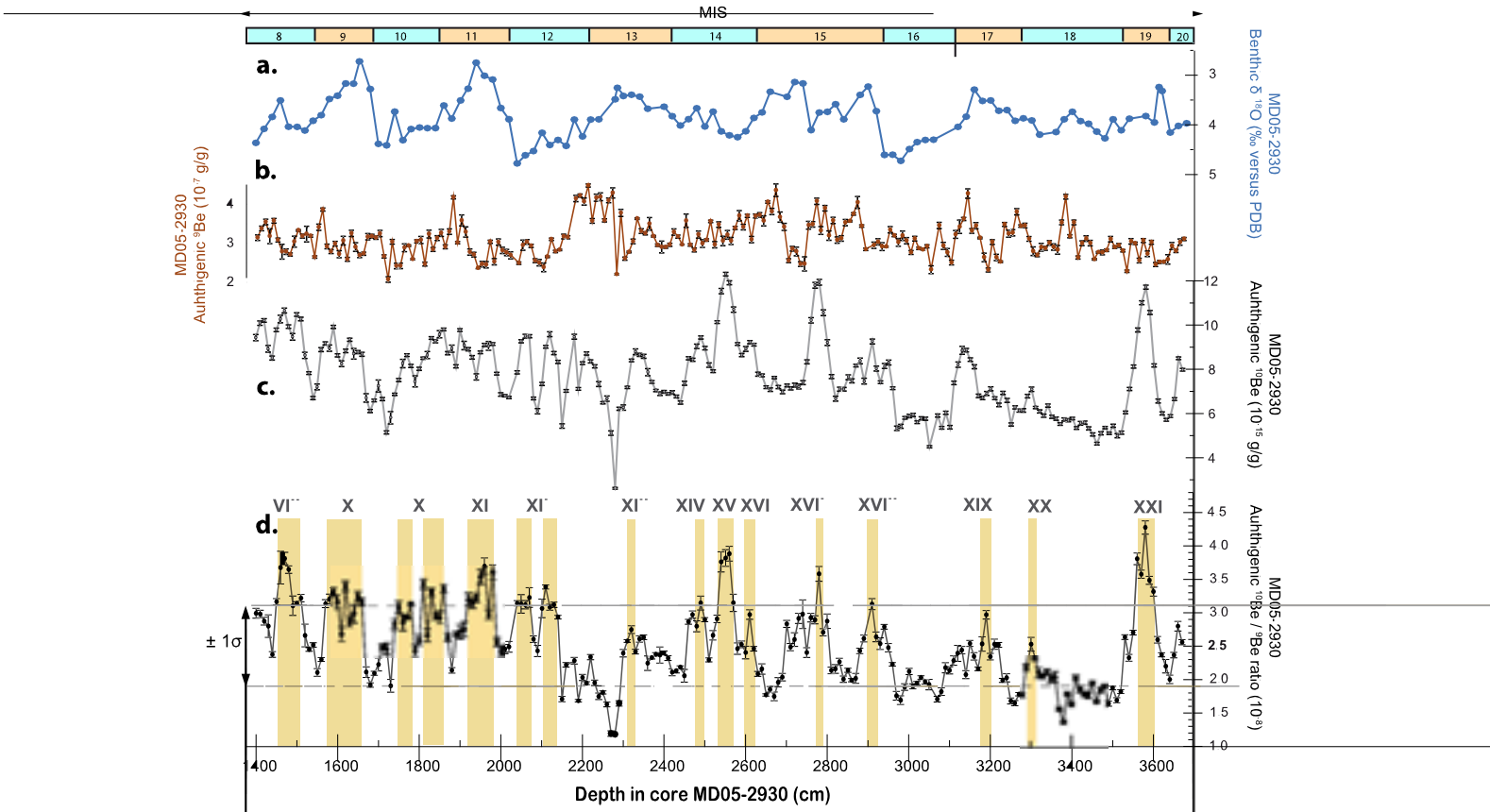

Fig. 3. Geochemical and paleomagnetic proxies measured along core MD05-2930 depth scale: (a) benthic $\delta^{18}O$ record with identified Marine Isotope Stages (MIS). (b) authigenic ^{9}Be concentrations with 1σ uncertainty. (c) Decay-corrected authigenic ^{10}Be concentrations with 1σ uncertainty. (d) Decay-corrected authigenic $^{10}Be/^{9}Be$ ratios with 1σ uncertainty. Dotted lines delimit the ± 1-sigma envelope of the distribution around the long-term mean value ($(2.51 \pm 0.04) \times 10^{-8}$). Authigenic $^{10}Be/^{9}Be$ enhancements are highlighted by the vertical yellow bars and numbered from VIII to XXI, following the labelling system proposed by Carcaillet et al. (2004a) (Interval VIII has been correlated with GDL "g"). (For interpretation of the references to colour in this figure, the reader is referred to the web version of this article.)

Table 2
Geomagnetic Dipole Lows (GDL) in the MD05-2930 record (expressed as $^{10}Be/^{9}Be$ increases), and corresponding GDL in the SINT-2000 and/or in the PISQ-1500 records.

$^{10}Be/^{9}Be$ enhancements labels	Depth (cm)	Depth of the $^{10}Be/^{9}Be$ maxima (cm)	Age of the $^{10}Be/^{9}Be$ maxima (ka)	Enhancement factors vs. longterm average (vs. framing values)	Marine isotope stages	GDL label*
VIII	1440–1520	1470	~ **285**	**1.5** (1.7)	8	**g**
IX	1570–1660	1590; 1620; 1650	~ **313;** ~ **319;**	**1.3** (1.6)	9	**h**
X	1740–1860	1810; 1830; 1860	~ **326** ~ **367;**	**1.25** (1.55)	10	**i1**
XI	1900–1980	1960	~ **372;** ~ **380**	**1.5** (1.5)	11	**i2**
XII	2030–2140	2070; 2110	~ **406**	**1.3** (1.6)	12	**j**
XIII	2310–2360	2320	~ **439;**		13	**k**
XIV	2460–2500	2490	~ **447**	**1.25** (1.5)	14	**l1**
XV	2530–2570	2560	~ **493**	**1.55** (2.0)	14	**l2**
XVI	2600–2620	2610	~ **52**	**1.2** (1.45)	14	**m**
XVII	2700–2810	2780	**5**	**1.4** (1.7)	15	**n**
XVIII	2880–2960	2910	~ **54**	**1.25** (1.6)	15	**o**
XIX	3090–3220	3190	**0**	**1.2** (1.6)	17	**p, q**
XX	3290–3380	3300	~ **55**	(1.4)	18	**r**
XXI	3550–3600	3580	**3**	**1.7** (2.5)	19	**s**
			~ **58**			
			8			
			~ **61**			
			5			
			~ **71**			
			0			
			~ **77**			
			5			

* According to a nomenclature proposed by Thouveny et al. (2008).

(~ 1.5-fold increase). These two intervals match the double structure of GDL i documented in PISO-1500 (Fig. 3) and agree with repeated RPI minima documented at 368, at 402 and at 413 ka in equatorial Pacific sediments (Valet and Meynadier, 1993). Although GDL i consists of a single VDM depletion in SINT-2000, the multiple structure of intervals X and XI is compatible with the identification of several excursions in the 360–0420 ka interval (Langereis et al., 1997; Lund et al., 2001;
Channell et al., 2012).

– Interval XII documents two ^{10}Be production rate enhancements (1.3-fold increase) at ~ 435 and ~ 450 ka, respectively, which confirm the double structure of GDL j in PISO-1500 (j1 at 430–445 ka and j2 at 455–460 ka), instead of a single GDL j, as reported in SINT-2000.
– Interval XIII at ~ 490–500 ka is hardly significant compared with the long-term average, but correlates with GDL k, a wide GDL of small amplitude in SINT-2000 and a narrow GDL of
large amplitude in PISO-1500. It is emphasized by the weakest $^{10}Be/^{9}Be$ ratio value of the whole record, at 485 ka, which

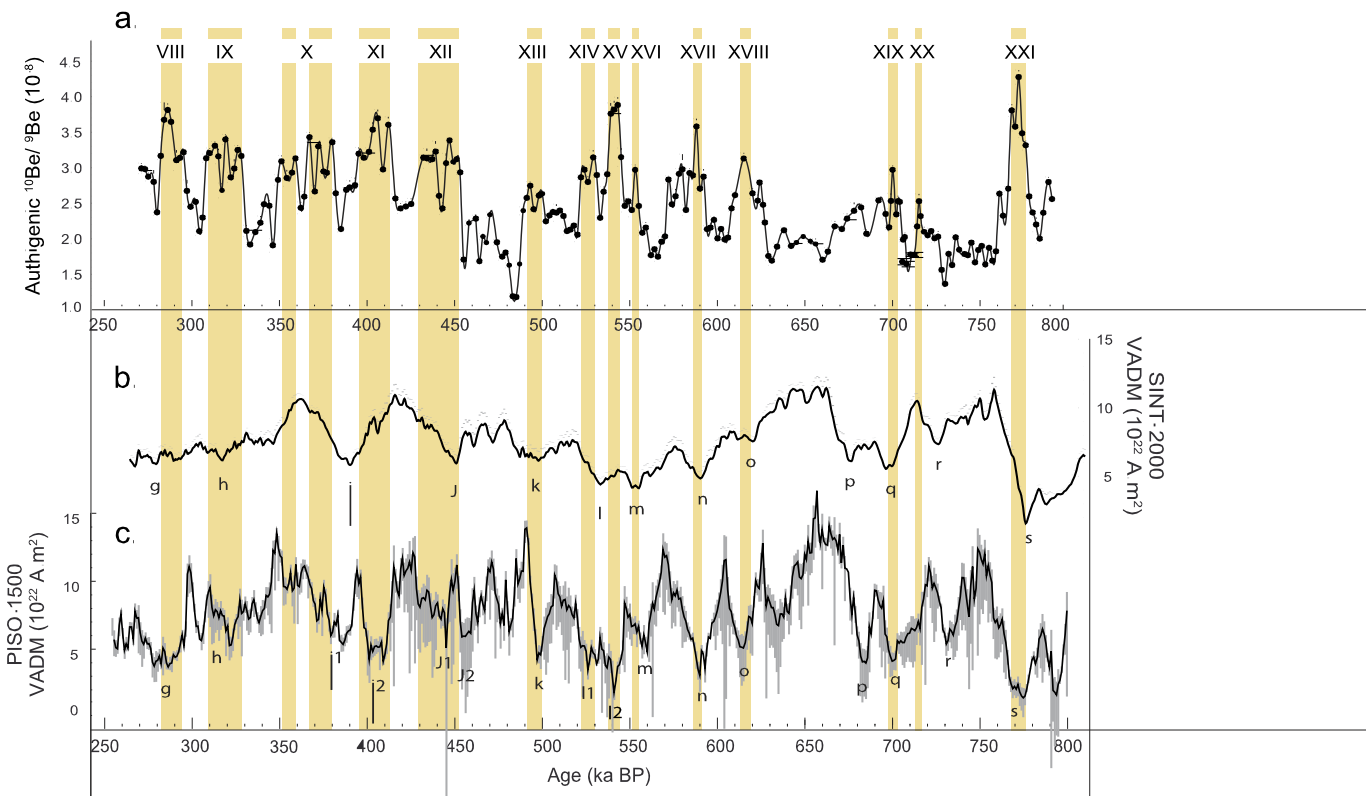

Fig. 4. Comparison of the MD05-2930 authigenic ^{10}Be/^{9}Be record with VADM reconstructions obtained from RPI stacks. All records are plotted on their own respective time scales. (a) MD05-2930 authigenic ^{10}Be/^{9}Be record; (b) SINT-2000 (Valet et al., 2005) and (c) PISO-1500 (Channell et al., 2009). Authigenic ^{10}Be/^{9}Be enhancements (numbered from VIII to XXI) are highlighted by the vertical yellow bars and correspond to Geomagnetic Dipole Lows (GDL) identified in the VADM records. The GDL nomenclature established for SINT-800 in Thouveny et al. (2008) has been applied to PISO-1500. (For interpretation of the references to colour in this figure, the reader is referred to the web version of this article.)

documents a high transient VDM phase recorded in PISO immediately after GDL k.

– Three Intervals have been identified in a massive structure recorded between 520 and 560 ka and have been labelled XIV (*522–529* ka), XV (*539–544* ka) and XVI (*554* ka). They document three distinct ^{10}Be overproductions responding to GDL l and m in SINT-2000, and to GDL l1, l2, and m in PISO-1500 at ~ 520 ka, ~ 540 ka and ~ 560 ka, respectively. Interval XV is among the three highest ^{10}Be overproductions of the
250–800 ka time interval (1.55-fold increase compared to the long term average). It responds to GDL l2 of PISO-1500, the most pronounced GDL of the whole Brunhes epoch.

Excursions recorded between 480 and 520 ka in oceans sediments (Langereis et al., 1997; Lund et al., 2001; Channell et al. 2004, 2012), and in lava flows from the Eifel volcanic field (Germany) (Schnepp and Hradetzky, 1994; Singer et al., 2008) correlate with intervals XIV and XV and GDL I1 and l2.

Between 550 and 575 ka a short reversed event recorded in lava flows from Idaho was dated at 565 ± 14 ka (Champion et al., 1988), then at 550 ± 10 ka (Champion et al., 1996), and finally at 558 ± 20 ka (Lanphere, 2000). Low paleointensities and anomalous paleomagnetic directions were also recorded in lavas from the Eifel (Germany), dated at 555 ± 4 ka (Singer et al., 2008). ODP sites 1060 to 1063 (northwest Atlantic) also revealed excursions at ~ 575 ka (Lund et al., 2001; Channell et al., 2012).

– Interval XVII at *585–590* ka documents a 1.4-fold enhanced ^{10}Be production rate emerging from a massive signature. This sharp signal at ~ 588 ka correlates with GDL n documented at 590–600 ka in both SINT-2000 and PISO-1500. Excursional directions and RPI lows at roughly this age were reported from ODP sites 983 and 984 (Channell et al., 2004) and ODP leg 172 (Lund et al., 2001) sediments. Other evidences of excursion were reported from lavas of La Palma (Canary) Island, dated at 602 ± 24 ka (Quidelleur et al., 1999) and at 580 ± 8 ka (Singer et al., 2002), and from lavas of the Eifel (Germany) and from Tahiti, dated at 578 ± 8 and 579 ± 6 ka, respectively (Singer et al., 2008).

– Interval XVIII at 610–625 ka documents a 1.25-fold ^{10}Be production rate increase event centred at 615 ka that responds to a GDL recorded sharply at 615 ka in PISO-1500 and expressed smoothly at ~ 625 ka in SINT-2000. The only evidences of an excursion at this age come from anomalous directions in a loess sequence (Liu et al., 1988). The secondary dipole low (unlabelled) recorded at 635 ka in the PISO-1500 and absent
from SINT-2000 is not confirmed by the cosmogenic Be record.

– Interval XIX documents a small ^{10}Be overproduction between 670 and 705 ka which is maximized at 700 ka, and which may respond to GDL q in both SINT-2000 and PISO-1500. There is no significant ^{10}Be enhancement at 670–680 ka that could be related to GDL p. Interval XIX and GDL q can be related to a double excursional feature recorded in sediments deposited during MIS 17 in Osaka Bay (Biswas et al., 1999) and also reported from ODP sites 983 and 984 (Channell et al., 2004).

– Interval XX at 715–725 ka is hardly significant and has no counterpart in SINT-2000 and in PISO-1500, where GDL r is recorded at 730 ka.

– Last but not least, Interval XXI documents the largest ^{10}Be enhancement of the whole record. Its closeness to the largest RPI low and the declination swing helps to unambiguously identify it with the cosmogenic response to the GDL s, i.e. the dipole field collapse linked with the Brunhes–Matuyama (B/M) reversal. It consists of a 1.7-fold increase of the ^{10}Be production

Table 3
Average values of the clusters computed from GDM and $^{10}Be/^{9}Be$ datasets using 3 strategies.

GDM (10^{22} A m^2)		Authigenic $^{10}Be/^{9}Be$ (10^{-8})	
Strategy 1:			
Values $< \mu_g - 2\sigma_g$:	1.31 ± 0.43	Values $> \mu_c + 2\sigma_c$:	3.77 ± 0.09
$\mu_g - 2\sigma_g <$ Values $> \mu_g + 2\sigma_g$:	7.53 ± 2.67	$\mu_c - 2\sigma_c <$ Values $> \mu_c + 2\sigma_c$:	2.47 ± 0.52
Values $> \mu_g + 2\sigma_g$:	16.08 ± 2.67	Values $< \mu_c - 2\sigma_c$:	1.19 ± 0.01
Strategy 2:			
Values $< \mu_g - 1\sigma_g$:	0.93 ± 0.32	BM $^{10}Be/^{9}Be$ maximum value:	4.28 ± 0.10
$\mu_g - 1\sigma_g <$ Values $> \mu_g + 1\sigma_g$:	5.19 ± 2.42	$\mu - 1\sigma <$ Values $> \mu + 1\sigma$:	2.61 ± 0.65
Values $> \mu + 1\sigma$:	11.15 ± 1.85	Values $< \mu - 1\sigma$:	1.90 ± 0.16
Strategy 3:			
Values $< \mu_g - 2\sigma_g$:	0.61 ± 0.33	BM $^{10}Be/^{9}Be$ maximum value:	4.28 ± 0.10
$\mu_g - 2\sigma_g <$ Values $> \mu_g + 2\sigma_g$:	7.34 ± 2.86	$\mu_c - 2\sigma_c <$ Values $> \mu_c + 2\sigma_c$:	2.46 ± 0.54
Values $> \mu_g + 2\sigma_g$:	16.08 ± 2.67	Values $< \mu_c - 2\sigma_c$:	1.19 ± 0.01

(μ_c; σ_c): parameters of the cosmogenic distribution (Be ratios)
(μ_g; σ_g): parameters of the geomagnetic distribution (absolute GDM values)
For each strategy, $\mu_{g,c}$ are given in the text with their associated uncertainty (standard deviation of the mean), and $\sigma_{g,c}$ are the standard deviation of the distributions.
BM: Brunhes–Matuyama transition.

rate compared to the long-term average. The production rate maximum recorded at ~ 773 ka coincides perfectly with the minimum of PISO-1500 at ~ 770–775 ka and agrees satisfac-torily with the minimum of SINT-2000 at ~ 777 ka. The am-plitude of the presented $^{10}Be/^{9}Be$ peak is consistent with a doubling of the ^{10}Be production rate during the B/M transi-
tion reported from marine sediments (Raisbeck et al., 1985; Carcaillet et al., 2003) and from an ice sheet (Raisbeck et al., 2006). The MD05-2930 record stops at 791 ka and thus does not cover the period preceding the B/M polarity transition, and notably the GDL precursor of the B/M revealed by sev-eral studies (e.g. Channell et al., 2009; Singer et al., 2005), among which the MD97-2140 $^{10}Be/^{9}Be$ record (Carcaillet et al. 2003, 2004b) showed a maximum centred at ~ 772 ka and a second and less pronounced peak at ~ 795 ka, relative to this precursor.

The authigenic $^{10}Be/^{9}Be$ record of core MD05-2930 suggests that numerous ^{10}Be overproduction events occurred throughout the 250–800 ka time period. Eight of these events (occurring at ~ 285 ka, ~ 320 ka, ~ 370 ka, ~ 410 ka, ~ 445 ka, ~ 540 ka, ~ 590 ka) represent 70 to 90% of the overproduction recorded during the B/M reversal. The presented record indicates that the global cosmogenic nuclide production rate increases by a factor
of 1.6 to 2 during major dipole moment collapses (at ~ 540 and ~ 773 ka). All ^{10}Be production enhancements represent 1.4 to 2-fold increases compared to the values of the framing depth inter-vals. It should be emphasized that these $^{10}Be/^{9}Be$ increase factors
were obtained with a temporal resolution of one measurement ev-ery 2000 yr, which implies that even the sharpest signatures are probably smoothed (see Christl et al., 2007; Ménabréaz et al., 2012).

5. Calibration and transfer to ^{10}Be-derived Dipole Moments

The obtained authigenic $^{10}Be/^{9}Be$ ratio record results at the first order from variations of the atmospheric cosmogenic ^{10}Be produc-tion, modulated at the global scale by the Geomagnetic Dipole Moment (GDM) variations. Calibration of the $^{10}Be/^{9}Be$ ratio scale using the absolute GDM values that modulated production over the studied time period (see also Ménabréaz et al., 2011 and 2012) is therefore justified.

The absolute GDM values consist of 437 Virtual Dipole Mo-ments (VDM) or Virtual Axial Dipole Moments (VADM) extracted from the absolute paleointensity database PINT-08 (Biggin et al., 2010, http://earth.liv.ac.uk/pint/) for the studied time period. This calibration procedure must account for uncertainties inherent to volcanic paleomagnetic data, thus we have associated clusters of high, intermediate and low GDM values with clusters of low, medium and high values of the $^{10}Be/^{9}Be$ ratio using different strategies. The cluster data are listed in Table 3 and presented in Fig. 5.

Strategy 1 excludes the data of the Brunhes–Matuyama tran-sition. This leads to the following time-averaged values: GDM = $(7.93 \pm 0.17) \times 10^{22}$ A m^2; authigenic $^{10}Be/^{9}Be = (2.48 \pm 0.04) \times 10^{-8}$. These time-averaged values are used to discriminate the data that are comprised between "mean $\pm 2\sigma$" from data that are either higher than "mean $+2\sigma$" or lower than "mean -2σ" (Table 3).

Strategy 2 concentrates on the Brunhes–Matuyama transition: an average GDM value of $(5.27 \pm 0.37) \times 10^{22}$ A m^2 and an average authigenic $^{10}Be/^{9}Be$ value of $(2.80 \pm 0.17) \times 10^{-8}$ were calculated over the 700–800 ka time interval, which accounts for dating un-certainties of the volcanic records and incorporates a suffi cient number of data points to be representative. The clusters were de-fined using the "mean $\pm 1\sigma$" limits (Table 3) because no $^{10}Be/^{9}Be$ values were lower than "mean -2σ".

Finally, these two calibration approaches separating non-transitional from transitional geomagnetic states were com-pared using Strategy 3, established over the whole studied time in-terval, which leads to the following time-averaged values: GDM = $(7.32 \pm 0.18) \times 10^{22}$ A m^2; $^{10}Be/^{9}Be = (2.51 \pm 0.04) \times 10^{-8}$ (Ta-ble 3).

The calibration points obtained using all cluster strategies are used to construct an empirical calibration curve (Fig. 5A). Since the relationship between geomagnetic field modulation and ^{10}Be production rate is non-linear, the calculation of arithmetic means inside the clusters introduces slight errors that are probably in-cluded in the error bars expressed in Fig. 5. Time-averaged GDM values including and excluding the B/M transition values ($(7.32 \pm 0.18) \times 10^{22}$ A m^2 and $(7.93 \pm 0.17) \times 10^{22}$ A m^2 respectively) are also represented in Fig. 5A. The polynomial regression that pro-vides the best fit through the calibration points (Fig. 5A) agrees with the calibration curve previously obtained over the 20–50 ka interval, including the ^{10}Be overproduction produced by the GDL of the Laschamp excursion (Ménabréaz et al., 2012) (Fig. 5B). Even if this agreement confirms that the signal recorded in different sed-iment archives results from a global-scale modulation, the most reliable inter-calibration will be furnished by the direct compari-son of the cosmogenic production signatures obtained for the same geomagnetic event at different sites: the future study of the up-per part of the MD05-2930 sequence will allow us to compare and better calibrate the records of the overproduction due to the Laschamp GDL.

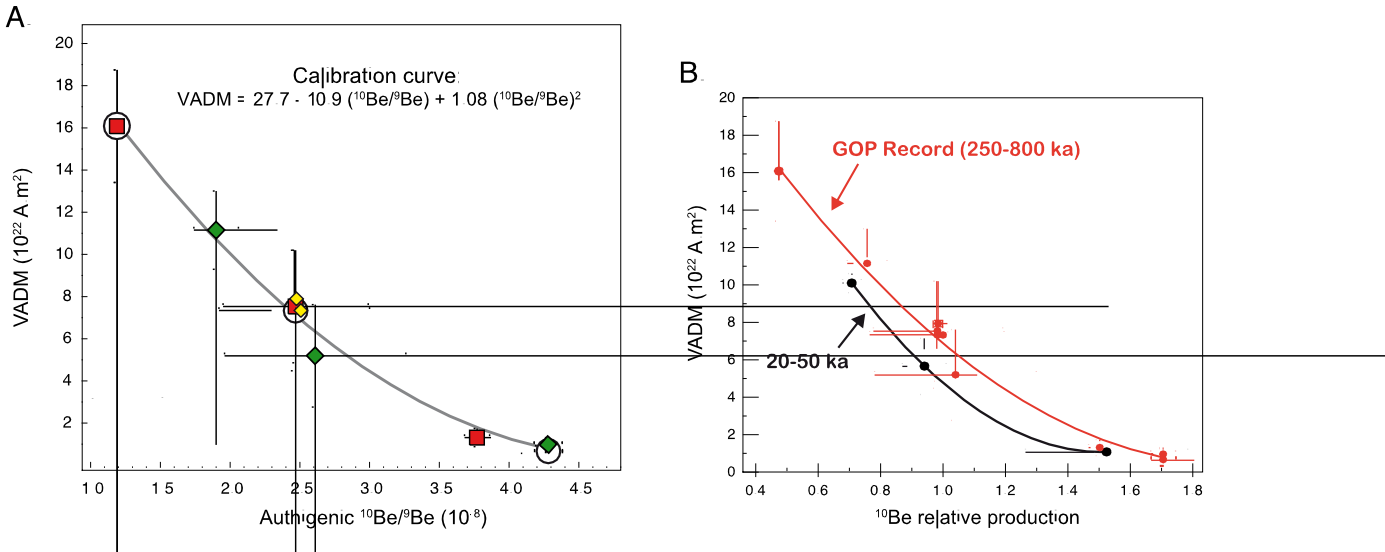

Fig. 5. Calibration method of the authigenic $^{10}Be/^{9}Be$ record (proxy of the global ^{10}Be production rate variations) using absolute VADM values extracted from the PINT-08 database. (A) Average VADM (10^{22} A m^2) and Authigenic $^{10}Be/^{9}Be$ (10^{-8}) values computed for the different clusters (see text). White circles represent the cluster values computed over the complete time interval studied (strategy 3). Red squares are the calibration clusters obtained over the studied time interval, excluding Brunhes–Matuyama (strategy 1). Green diamonds represent the cluster values computed over the Brunhes–Matuyama transition only (strategy 2). Associated error bars correspond to the standard deviation of the values used in each cluster. The polynomial fit between these calibration points is used to compute the Be-derived Geomagnetic dipole moment record: $VADM = 27.70 - 10.93 \times (^{10}Be/^{9}Be) + 1.075 \times (^{10}Be/^{9}Be)^2$. The small yellow diamonds mark the $^{10}Be/^{9}Be$ and VADM time averages calculated over the whole studied time interval. (B) The calibration curve of the MD05-2930 (GOP = Gulf of Papua) (red line and symbols) plotted beside the calibration curve of the 20–50 ka time interval (black line and symbols) computed from the Portuguese margin and Papua New Guinea margin records, including the Laschamp excursion (Ménabréaz et al., 2012). The authigenic $^{10}Be/^{9}Be$ ratios measured along core MD05-2930 were normalized to their own average value ($(2.51 \pm 0.04) \times 10^{-8}$). (For interpretation of the references to colour in this figure, the reader is referred to the web version of this article.)

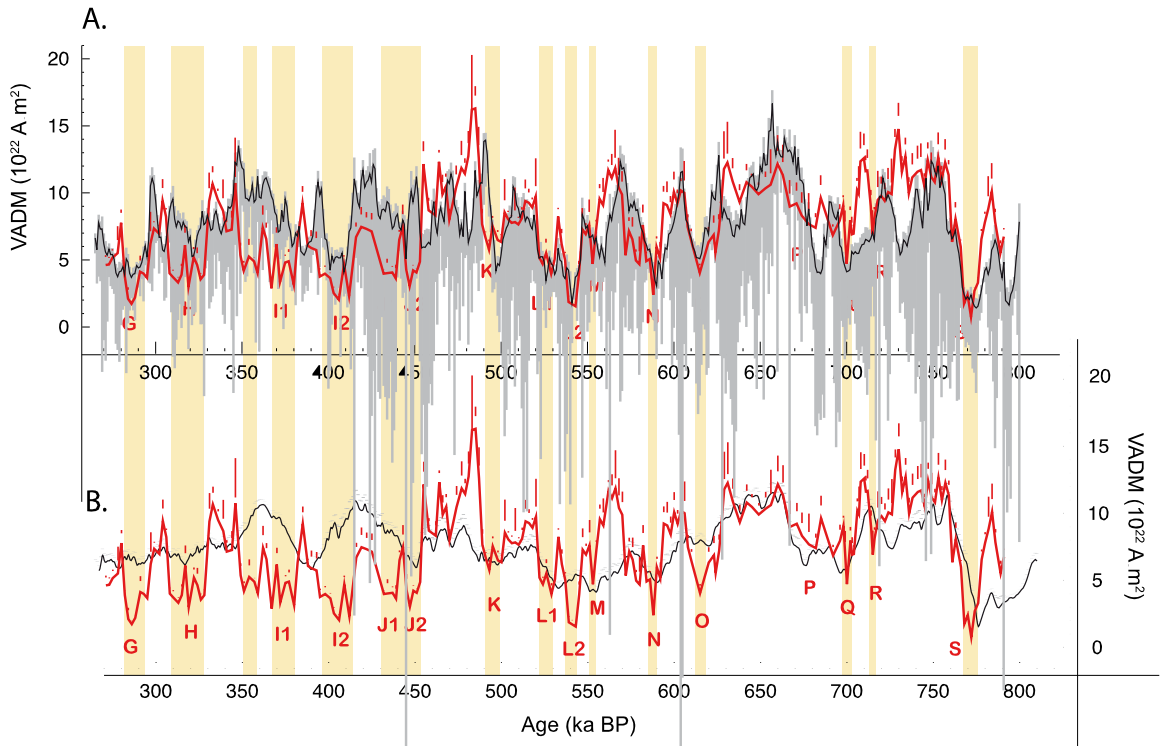

Fig. 6. Paleomagnetic VADM (black curves) and cosmogenic-derived GDM (red curve) reconstructions of the 250–800 ka interval plotted on their own respective time scales. The ^{10}Be-derived GDM record is compared to (A) the PISO-1500 VADM record (Channell et al., 2009) and (B) the SINT-2000 VADM record (Valet et al., 2005). The geomagnetic dipole lows (GDL) documented by the ^{10}Be-derived VADM reconstruction are labelled from G to S and highlighted by the yellow vertical bars. (For interpretation of the references to colour in this figure, the reader is referred to the web version of this article.)

Table 4
Virtual Axial Dipole Moments (VADM) between 250 ka and 800 ka, reconstructed from the Authigenic $^{10}Be/^{9}Be$ ratios measured along Core MD05-2930.

Age (ka BP)	VADM (10^{22} A m^2)*	Age (ka BP)	VADM (10^{22} A m^2)*	Age (ka BP)	VADM (10^{22} A m^2)*	Age (ka BP)	VADM (10^{22} A m^2)*	Age (ka BP)	VADM (10^{22} A m^2)*
271	4.63 ± 0.75	388	6.09 ± 0.55	508	7.68 ± 0.58	608	6.48 ± 0.90	734	12.74 ± 1.41
273	4.67 ± 0.57	390	5.92 ± 1.34	510	8.13 ± 0.85	615	4.03 ± 0.70	736	10.01 ± 1.19
275	5.17 ± 0.65	393	5.76 ± 1.39	512	9.43 ± 1.61	620	6.35 ± 1.16	738	11.18 ± 1.82
278	5.53 ± 2.02	395	3.74 ± 0.64	514	9.30 ± 1.05	623	6.89 ± 1.47	741	11.61 ± 1.96
280	7.81 ± 0.99	398	3.97 ± 0.61	516	8.95 ± 0.74	624	5.58 ± 0.48	743	11.74 ± 2.00
282	3.88 ± 0.37	401	3.64 ± 0.41	518	9.77 ± 2.86	626	7.23 ± 1.23	745	10.52 ± 0.98
284	2.05 ± 0.84	403	2.49 ± 0.47	520	5.21 ± 0.44	627	8.69 ± 0.70	747	12.46 ± 1.35
286	1.66 ± 0.27	406	1.98 ± 0.42	522	4.71 ± 0.58	629	11.81 ± 2.82	749	11.23 ± 1.84
288	2.14 ± 0.21	409	4.70 ± 0.67	524	5.53 ± 1.07	631	12.28 ± 3.05	751	10.84 ± 1.03
291	4.12 ± 1.20	412	2.27 ± 0.46	526	3.96 ± 0.84	634	10.90 ± 1.73	753	12.68 ± 1.86
293	3.98 ± 0.23	416	6.73 ± 1.11	529	5.06 ± 0.42	638	9.36 ± 1.32	755	11.00 ± 1.06
295	3.65 ± 0.41	419	7.50 ± 1.49	531	8.28 ± 0.65	642	10.83 ± 1.37	757	12.30 ± 1.75
297	6.23 ± 2.39	422	7.35 ± 1.26	533	6.22 ± 1.13	645	10.50 ± 0.98	759	11.36 ± 1.13
299	7.37 ± 0.55	425	7.16 ± 1.38	535	5.00 ± 0.62	649	9.94 ± 0.88	761	6.36 ± 0.58
302	6.99 ± 0.67	432	3.97 ± 0.31	537	1.80 ± 0.46	653	10.37 ± 1.27	763	8.10 ± 1.26
304	9.45 ± 1.62	434	4.01 ± 1.08	539	1.64 ± 0.34	656	10.64 ± 2.66	766	6.01 ± 0.54
306	8.26 ± 0.65	437	4.07 ± 0.49	541	1.47 ± 0.26	663	12.19 ± 2.15	768	1.67 ± 0.24
308	4, 00 ± 0.46	439	3.62 ± 1.01	543	3.94 ± 0.98	667	11.38 ± 2.26	770	2.36 ± 0.28
310	3.71 ± 0.56	441	6.53 ± 0.74	545	7.31 ± 1.61	671	9.01 ± 1.99	772	0.62 ± 0.09
313	3.30 ± 0.42	443	7.50 ± 1.67	547	6.95 ± 0.83	674	9.25 ± 1.56	774	2.67 ± 0.28
315	3.89 ± 0.81	445	4.30 ± 1.18	549	7.64 ± 1.91	678	8.34 ± 1.76	776	3.28 ± 0.42
317	6.12 ± 1.51	447	3.02 ± 0.17	551	4.71 ± 0.77	682	7.70 ± 2.33	778	6.57 ± 0.76
319	2.97 ± 0.42	449	4.23 ± 0.42	553	7.31 ± 0.72	685	7.43 ± 1.10	780	7.84 ± 0.80
322	5.21 ± 0.77	451	4.07 ± 0.32	555	9.59 ± 1.11	688	9.66 ± 1.69	782	8.86 ± 2.43
324	4.64 ± 1.31	453	4.88 ± 0.30	557	9.12 ± 2.03	692	6.88 ± 0.82	784	10.13 ± 2.13
326	3.54 ± 0.46	455	12.17 ± 1.71	559	11.73 ± 0.80	696	7.97 ± 1.23	786	7.86 ± 1.00
328	3.88 ± 0.45	458	8.73 ± 0.95	562	11.14 ± 1.81	698	9.10 ± 0.76	789	5.54 ± 0.95
331	9.41 ± 2.14	462	8.36 ± 1.10	564	11.88 ± 2.86	699	6.92 ± 1.81	791	6.77 ± 0.64
333	10.69 ± 1.34	464	12.35 ± 0.89	566	10.42 ± 2.24	700	4.72 ± 0.67	mean ± std. dev.	7.42 ± 3.12
336	9.53 ± 0.82	466	9.93 ± 1.47	568	9.91 ± 1.76	702	8.00 ± 1.03	mean ± SDOM	7.42 ± 0.21
339	8.70 ± 2.35	468	10.51 ± 0.98	570	5.36 ± 0.69	703	6.94 ± 1.32		
341	7.17 ± 0.87	470	8.03 ± 0.83	572	7.18 ± 1.04	704	6.99 ± 0.67		
344	7.29 ± 1.43	472	10.47 ± 1.62	574	6.56 ± 1.67	706	10.22 ± 0.93		
346	10.77 ± 3.39	474	11.88 ± 2.04	576	4.98 ± 0.82	707	9.97 ± 2.07		
349	5.38 ± 0.92	477	11.46 ± 1.15	578	4.69 ± 2.08	708	12.37 ± 2.22		
351	4.20 ± 0.74	479	12.76 ± 1.88	580	7.64 ± 1.53	710	12.62 ± 1.84		
354	5.26 ± 1.33	481	16.21 ± 4.09	582	4.92 ± 0.71	711	11.65 ± 1.18		
357	4.90 ± 0.31	483	16.3 ± 1.66	584	5.08 ± 0.64	712	11.70 ± 1.59		
359	4.02 ± 0.24	485	12.64 ± 2.31	586	2.35 ± 0.48	714	9.02 ± 1.25		
362	7.45 ± 1.66	487	7.69 ± 1.16	588	5.99 ± 0.80	715	6.94 ± 1.82		
364	6.59 ± 1.23	489	6.68 ± 0.47	590	5.17 ± 1.19	716	8.14 ± 0.85		
367	2.86 ± 0.35	491	5.79 ± 0.76	592	9.26 ± 1.30	718	9.51 ± 2.18		
370	6.21 ± 1.26	493	7.56 ± 0.76	594	9.12 ± 1.78	720	9.82 ± 1.44		
372	3.33 ± 0.37	495	6.51 ± 0.75	596	8.46 ± 1.34	722	9.44 ± 1.35		
375	4.82 ± 0.59	498	6.37 ± 0.59	598	10.11 ± 1.51	724	10.09 ± 1.81		
377	4.91 ± 0.91	500	8.58 ± 2.50	600	9.25 ± 1.04	726	9.95 ± 2.65		
380	3.11 ± 0.34	502	8.08 ± 0.63	602	10.21 ± 0.92	728	13.26 ± 1.53		
382	6.34 ± 0.87	504	7.79 ± 0.59	604	10.03 ± 2.39	730	14.78 ± 1.95		
385	9.25 ± 1.30	506	7.86 ± 2.59	606	7.50 ± 0.93	732	11.6 ± 1.17		

* Uncertainties (2σ) result from the propagation of analytical uncertainties only, and are rounded to the higher value.

The application of the equation derived from Fig. 5A to the $^{10}Be/^{9}Be$ ratio record provides the ^{10}Be-derived GDM record presented in Fig. 6 and Table 4.

6. Discussion

6.1. Time-varying dipole moment between 250 and 800 ka

The obtained ^{10}Be-derived GDM (Fig. 6) oscillates around an average value of 7.4×10^{22} A m^2 (standard deviation: 3.1×10^{22} A m^2), close to the present dipole field strength value of 7.78×10^{22} A m^2, and consistent with the average value of $(7.5 \pm 1.7) \times 10^{22}$ A m^2 calculated by Valet et al. (2005) for the Brunhes Chron. The ^{10}Be-derived GDM varies from 0.7 to 16.3×10^{22} A m^2.

Over the 250–800 ka interval, the ^{10}Be-derived GDM can be compared with the paleomagnetic reference records SINT-2000 (Valet et al., 2005) and PISO-1500 (Channell et al., 2009) (Fig. 6). It presents a series of Geomagnetic Dipole Lows (GDL), labelled from "G" to "S", in agreement with the paleomagnetic GDL labelled from "g" to "s" discussed in Section 4 and related to paleomagnetic excursions.

Despite independent methodologies applied to very different archives and using different calibration procedures (see Valet et al., 2005 and Channell et al., 2009 for details about the stack calibrations), the results are highly compatible. This strongly supports the global validity of the ^{10}Be-reconstruction, via a common primary signal modulation by the geomagnetic dipole. The amplitude of the ^{10}Be-derived GDM signal is similar to that of PISO-1500, i.e. higher than that of SINT-2000, itself higher than that of the PAD2M2 (Ziegler et al., 2011, data not shown here). Over this time interval, the detailed features visible in PISO-1500 are broadly confirmed in our record, with some chronological offsets and slightly lower VADM values before 450 ka. Possible age offsets may only result from individual age model uncertainties, and/or variable magnetization lock-in depths. Indeed, in such high particle flux environment, an assumed mean oceanic residence time of Be of about 600 yr (e.g. Raisbeck et al., 1980; Von Blanckenburg et al., 1996) do not allow to explain the observed offsets on the order of 5000–10 000 yr. Similarly, in such high sedimentation rate envi-

ronment, according to Christl (2007), an integration time of the Be signal over 1000 yr due to bioturbation would lead to time lags of about 600 yr. Consequently, the ^{10}Be signal does not suffer from delays as significant as suspected for magnetization lock-in depths, and the age of the main features linked to GDL recorded by the authigenic ^{10}Be/^{9}Be must be considered as more reliable.

The limited amplitude of several GDL is supported in this record. Indeed, the ^{10}Be-derived GDM values hardly ever appear lower than $\sim 5 \times 10^{22}$ A m^2 for GDL P, Q and R between 750 and 600 ka and for GDL K at ~ 490 ka. It should be mentioned that the ^{10}Be production record resolution may be improved, although
bioturbation may impose a limit by dampening the signal over its effi cient depth.

A critical value of GDM that trigger excursions or reversals was estimated by Channell et al. (2009) at $\sim 2.5 \times 10^{22}$ A m^2, i.e. 30% of the present GDM value. In the ^{10}Be-derived GDM record, only a few GDL reach this critical value: GDL G (~ 285 ka),
GDL I2 (390–410 ka), GDL L (520–550 ka) and the Brunhes–Matuyama transition (773 ka), which is characterized by a near-zero GDM value. The other GDL leading to excursions reached $\sim 3–4 \times 10^{22}$ A m^2, i.e. 50% of the present VDM value. Further cal-ibration improvements will allow to refine these quantifications,
and to establish a classification of critical GDM states required to trigger reversals, to trigger globally recorded excursions, or to allow the emergence of strong non-dipole field anomalies.

6.2. Chronological implications of ^{10}Be-derived dipole moment records

The age of ~ 773 ka obtained for the ^{10}Be-derived GDM min-imum related to the B/M reversal is consistent with the ages de-rived from astronomical calibrations of RPI records in sediment se-quences: 775 ± 2 ka (Bassinot et al., 1994), ~ 775 ka (Channell and Klevein, 2000), and is slightly younger than ~ 780 ka (Shackleton
et al., 1990) and 778.0 ± 1.7 ka (Tauxe et al., 1996). It is also fully consistent with both the most recent ^{40}Ar/^{39}Ar age of 772 ± 11 ka obtained from Hawaiian lava flows (Singer et al., 2012), and with the age of 773 ± 1 ka (2σ) derived from the astronomical calibration of high-deposition rate sedimentary sequences from the North Atlantic ODP cores (Channell et al., 2010).

Since enhancements of the ^{10}Be production rate occur globally and are simultaneously recorded in natural archives, the ^{10}Be-derived GDL signatures can be used as tie points between sediment cores from all regions and between marine and polar ice-sheet records (e.g. Raisbeck et al., 2006; Dreyfus et al., 2008). In this scope, it is worth noting that in the MD05-2930 record, the ^{10}Be production maximum linked with the dipole moment minimum is recorded at the end of the MIS 19 benthic δ^{18}O expression (Fig. 3).

The community working with *in-situ*-produced cosmogenic nuclides for dating Earth's surface processes will be able to use ^{10}Be-derived GDM records for the correction of production rates. Indeed, due to their common dependence on the cosmic ray flux, the use of atmospheric ^{10}Be-derived GDM reconstructions would enable to link Terrestrial Cosmogenic Nuclides (TCN) production rate variations to the geomagnetic field strength. We thus suggest the adoption of the ^{10}Be-derived GDM reconstruction presented in this paper for the extrapolation of recent TCN production rates back into the geological past.

7. Conclusions and perspectives

The authigenic ^{10}Be/^{9}Be ratio record of core MD05-2930 reveals the variation of the atmospheric ^{10}Be global production rate between 250 and 800 ka, modulated by magnetospheric shielding. Calibration using absolute VADM values provides a continuous record of the ^{10}Be-derived geomagnetic dipole moment (GDM) variation covering the Brunhes–Matuyama transition, and the early to mid Brunhes epoch. The ^{10}Be-derived geomagnetic dipole lows (GDL) series is compatible with those derived from paleomagnetic reconstructions, confirming the occurrence and global influence of recurrent dipole lows, and their link with paleomagnetic excursions documented and dated in sedimentary and/or volcanic archives. This study allows to better evaluate the critical states of the geomagnetic moment triggering global excursions and/or reversals. For example, it shows that the geomagnetic dipole lows that triggered the excursions at ~ 285 ka, at 390–410 ka, and at 520–550 ka, all reached the critical value of $\sim 2 \times 10^{22}$ A m^2, i.e. the threshold reached at 41 ka at the time of the Laschamp event
(Ménabréaz et al., 2012), whereas the Brunhes–Matuyama reversal was triggered by a near-zero GDM value. All other GDL over the 250–800 ka interval reached only half of the present VDM value ($\sim 3–4 \times 10^{22}$ A m^2).

Since the authigenic ^{10}Be/^{9}Be signatures are recorded without significant delays, the ^{10}Be-derived GDL series constitute accurate and precise geomagnetic markers for construction of global scale correlations between paleoclimatic/paleoenvironmental time series. They also provide an appropriate tool for studying the phase relationships between geomagnetic dipole moment variations and orbital, or paleoclimatic, variations. For example, our results reveal the ^{10}Be signature of the Brunhes/Matuyama transition at ~ 773 ka, near the end of MIS 19.

Acknowledgements

This study is a contribution to the MAG-ORB project (ANR-09-BLAN-0053-01), which is funded by the French Agence Nationale de la Recherche (ANR). We greatly acknowledge V. Guillou for his contribution to chemical sample preparation and ^{9}Be measurements, F. Demory for his help during paleomagnetic measurements, C. Sonzogni for her help with isotope analysis and N. Buchet for foraminiferal picking. We thank J.J.-P. Valet, M. Frank and Tibor Dunai for acting as reviewers of L. Ménabréaz's PhD thesis, and for constructive discussions. We also thank M. Arnold, G. Aumaître, and K. Keddadouche for their invaluable assistance during ^{10}Be measurements at the ASTER AMS national facility (CEREGE, Aix-en-Provence), which is supported by the INSU/CNRS, the French Ministry of Research and Higher Education, the IRD and the CEA. Thanks are also due to the R.V. *Marion Dufresne* crew, and to the Chief scientist (L. Beaufort) and participants of MD148-PECTEN Cruise, which provided core MD05-2930. Pieter Vermeesch and two anonymous reviewers provided helpful comments to improve the manuscript.

References

Baroni, M., Bard, E., Petit, J.R., Magnan, O., Bourlès, D.L., 2011. Volcanic and solar activity, and atmospheric circulation influences on cosmogenic ^{10}Be fallout at Vostok and Concordia (Antarctica) over the last 60 years. Geochim. Cosmochim. Acta 75, 7132–7145, http://dx.doi.org/10.1016/j.gca.2011.09.002.

Bassinot, F.C., Labeyrie, L.D., Vincent, E., Quidelleur, X., Shackleton, N.J., Lancelot, Y., 1994. The astronomical theory of climate and the age of the Brunhes–Matuyama magnetic reversal. Earth Planet. Sci. Lett. 126, 91–108.

Beaufort, L., Chen, M.-T., Droxler, A.W., the Shipboard Scientific Party, 2005. MD148/PECTEN-IMAGES XIII Cruise Report. Inst. Polaire Fr. Paul Emile Victor, Brest, France.

Biggin, A.J., McCormack, A., Roberts, A., 2010. Paleointensity database updated and upgraded. EOS Trans. 91 (2).

Biswas, D.K., Hyodo, M., Tanigucchi, Y., 1999. Magnetostratigraphy of Pio-Pleistocene sediments in a 1700 m core from Osaka Bay, Southwestern Japan and short geomagnetic events in the middle Matuyama and the early Brunhes chrons. Palaeogeogr. Palaeoclimatol. Palaeoecol. 148, 233–248.

Bourlès, D.L., 1992. Beryllium isotopes in the earth's environment. In: Encyclopedia of Earth System Science, vol. 1, pp. 337–352.

Bourlès, D.L., Raisbeck, G.M., Yiou, F., 1989. ^{10}Be and ^{9}Be in marine sediments and their potential for dating. Geochim. Cosmochim. Acta 53, 443–452.

Carcaillet, J., Thouveny, N., Bourlès, D.L., 2003. Geomagnetic moment instability between 0.6 and 1.3 Ma from cosmonuclide evidence. Geophys. Res. Lett. 30 (15), 1792, http://dx.doi.org/10.1029/2003GL017550.

Carcaillet, J., Bourlès, D.L., Thouveny, N., Arnold, M., 2004a. A high-resolution authigenic $^{10}Be/^{9}Be$ record of geomagnetic moment variations over the last 300 ka from sedimentary cores of the Portuguese margin. Earth Planet. Sci. Lett. 219, 397–412.

Carcaillet, J., Bourlès, D.L., Thouveny, N., 2004b. Geomagnetic dipole moment and ^{10}Be production rate intercalibration from authigenic $^{10}Be/^{9}Be$ for the last 1.3 Ma. Geochem. Geophys. Geosyst. 5, 397–412, http://dx.doi.org/10.1029/2003GC000641. Q05006.

Champion, D.E., Lanphere, M., Anderson, S.R., 1996. Further verification and $^{40}Ar/^{39}Ar$ dating of the Big Lost reversed polarity subchron from drill core subsurface samples of the Idaho National Engineering Laboratory, Idaho. EOS Trans. AGU 77, F165.

Champion, D., Lanphere, M., Kuntz, M., 1988. Evidence for a new geomagnetic reversal from lava flows in Idaho: Discussion of short polarity reversals in the Brunhes and late Matuyama polarity chrons. J. Geophys. Res. 93 (B10), http://dx.doi.org/10.1029/88JB03323.

Channell, J.E.T., Curtis, J.H., Flower, B.P., 2004. The Matuyama–Brunhes boundary interval (500–900 ka) in north Atlantic drift sediments. Geophys. J. Int. 158, 489–505.

Channell, J.E.T., Hodell, D.A., Curtis, J.H., 2012. ODP Site 1063 (Bermuda Rise) revisited: Oxygen isotopes, excursions and paleointensity in the Brunhes Chron. Geochem. Geophys. Geosyst. 13 (G3), 1525–2027, http://dx.doi.org/10.1029/2011GC003897.

Channell, J.E.T., Kleiven, H.F., 2000. Geomagnetic paleointensities and astronomical ages for the Matuyama-Brunhes boundary and boundaries of the Jaramillo Subchron: palaeomagnetic and oxygen isotope records from ODP site 983. Philos. Trans. R. Soc. Lond. 358, 1027–1047.

Channell, J.E.T., Xuan, C., Hodell, D.A., 2009. Stacking paleointensity and oxygen isotope data for the last 1.5 Myr (PISO-1500). Earth Planet. Sci. Lett. 283, 14–23.

Channell, J.E.T., Hodell, D., McManus, J., Lehman, B., 1998. Orbital modulation of the Earth's magnetic field intensity. Nature 394, 464–468.

Channell, J.E.T., Hodell, D.A., Singer, B.S., Xuan, C., 2010. Reconciling astrochronological and $^{40}Ar/^{39}Ar$ ages for the Matuyama-Brunhes boundary and late Matuyama Chron. Geochem. Geophys. Geosyst. G3, 11, Q0AA12, http://dx.doi.org/10.1029/2010GC003203.

Chmeleff, J., von Blanckenburg F, Kossert, K., Jakob, D., 2010. Determination of the ^{10}Be half-life by multicollector ICP-MS and liquid scintillation counting. Nucl. Instrum. Methods Phys. Res., Sect. B, Beam Interact. Mater. Atoms 268, 192–199.

Christl, M., 2007. Sensitivity and response of beryllium-10 in marine sediments to rapid production changes (geomagnetic events): A box model study. Geochem. Geophys. Geosyst. 8, Q09015, http://dx.doi.org/10.1029/2007GC001598. 10 pp.

Christl, M., Mangini, A., Kubik, P.W., 2007. Highly resolved Beryllium-10 record from ODP Site 1089—A global signal?. Earth Planet. Sci. Lett. 257, 245–258.

Christl, M., Strobl, C., Mangini, A., 2003. Beryllium-10 in deep-sea sediments: a tracer for the Earth's magnetic field intensity during the last 200,000 years. Quat. Sci. Rev. 22, 725–739.

Christl, M., Lippold, J., Steinhilber, F., Bernsdorff, F., Mangini, A., 2010. Reconstruction of global ^{10}Be production over the past 250 ka from highly accumulating Atlantic drift sediments. Quat. Sci. Rev. 29, 2663–2672.

Coe, R.S., Liddicoat, J.C., 1994. Overprinting of natural magnetic remanence in lake sediments by subsequent high intensity field. Nature 367, 57–59.

Dickens, G.R., Droxler, A.W., Bentley, S.J., Peterson, L.C., Opdyke, B.N., Beaufort, L., Daniell, J., Febo, L.A., Francis, J.M., Harris, P.T., Jorry, S.J., Mallarino, G., McFadden, M., Muhammad, Z., Carson, B.E., Patterson, L., Tcherepanov, E., Zarikian, C.A., 2006. Sediment accumulation on the shelf edges, adjacent slopes, and basin floors of the Gulf of Papua: A preliminary late Quaternary view of sedimentary sinks in the Papua New Guinea Source-to-Sink focus area. Margins Newsl. 16, 1–5.

Dreyfus, G.B., Raisbeck, G.M., Parrenin, F., Jouzel, J., Guyodo, Y., Nomade, S., Mazaud, A., 2008. An ice core perspective on the age of the Matuyama–Brunhes boundary. Earth Planet. Sci. Lett. 274, 151–156.

Elsasser, W., Ney, E.P., Winckler, J.R., 1956. Cosmic-ray intensity and geomagnetism. Nature 178, 1226–1227.

Finkel, R.C., Nishiizumi, K., 1997. Beryllium 10 concentrations in the Greenland Ice Sheet Project 2 ice core from 3–40 ka. J. Geophys. Res. 102, 26699–26706.

Francis, J.M., Daniell, J.J., Droxler, A.W., Dickens, G.R., Bentley, S.J., Peterson, L.C., Opdyke, B.N., Beaufort, L., 2008. Deep water geomorphology of the mixed siliciclastic-carbonate system, Gulf of Papua. J. Geophys. Res. 113, f01s16, http://dx.doi.org/10.1029/2007jf000851.

François, R., Frank, M., Rutgers van der Loeff, M.M., Bacon, M.P., 2004. ^{230}Th normalization: An essential tool for interpreting sedimentary fluxes during the late Quaternary. Paleoceanography 19, 10–18.

Frank, M., Schwarz, B., Baumann, S., Kubik, P.W., Suter, M., Mangini, A., 1997. A 200 kyr record of cosmogenic radionuclide production rate and geomagnetic field intensity from ^{10}Be in globally stacked deep-sea sediments. Earth Planet. Sci. Lett. 149, 121–129.

Fuller, M., 2006. Geomagnetic field intensity, excursions, reversals and the 41,000-yr obliquity signal. Earth Planet. Sci. Lett. 245, 605–615.

Gee, J.S., Cande, S., Hildebrand, J., Donnelly, K., Parker, R., 2000. Geomagnetic intensity variations over the past 780 kyr obtained from near-seafloor magnetic anomalies. Nature 408, 827–832.

Guyodo, Y., Gaillot, P., Channell, J.E.T., 2000. Wavelet analysis of relative geomagnetic paleointensity at ODP site 983. Earth Planet. Sci. Lett. 184, 109–123.

Guyodo, Y., Valet, J.-P., 1999. Global changes in intensity of the Earth's magnetic field during the past 800 kyr. Nature 399, 249–252.

Harris, P.T., Baker, E.K., Cole, A.R., Short, S.A., 1993. A preliminary study of sedimentation in the tidally dominated Fly River delta, Gulf of Papua. Cont. Shelf Res. 13, 441–472.

Heikkilä, U., Beer, J., Feichter, J., 2009. Meridional transport and deposition of atmospheric ^{10}Be. Atmos. Chem. Phys. 9, 515–527.

Heikkilä, U., Beer, J., Abreu, J.A., Steinhilber, F., 2013. On the atmospheric transport and deposition of the cosmogenic radionuclides (^{10}Be): a review. Space Sci. Rev. 176, 321–332, http://dx.doi.org/10.1007/s11214-011-9838-0.

Henderson, G.M., Anderson, R.F., 2003. The U-series toolbox for paleoceanography. Rev. Mineral. Geochem. 52, 493–553.

Henken-Mellies, W.U., Beer, J., Heller, F., Hsü, K.J., Shen, C., Bonani, G., Hofmann, H.J., Suter, M., Wölfli, W., 1990. ^{10}Be and ^{9}Be in South Atlantic DSDP Site 519: Relation to geomagnetic reversals and to sediment composition. Earth Planet. Sci. Lett. 98, 267–276.

Hofmann, D., Fabian, K., 2009. Correcting relative paleointensity records for variations in sediment composition: Results from a South Atlantic stratigraphic network. Earth Planet. Sci. Lett. 284, 34–43.

Jorry, S.J., Droxler, A.W., Mallarino, G., Dickens, G.R., Bentley, S.J., Beaufort, L., Peterson, L.C., Opdyke, B.N., 2008. Bundled turbidite deposition in the central Pandora Trough (Gulf of Papua) since Last Glacial Maximum: Linking sediment nature and accumulation to sea level fluctuations at millennial timescale. J. Geophys. Res. 113, F01S19, http://dx.doi.org/10.1029/2006JF000649.

Knudsen, M.F., Henderson, G.M., Frank, M., Mac Niocaill, C., Kubik, P.W., 2008. In-phase anomalies in Beryllium-10 production and palaeomagnetic field behaviour during the Iceland Basin geomagnetic excursion. Earth Planet. Sci. Lett. 265, 588–599.

Korschinek, G., Bergmaier, A., Faestermann, T., Gerstmann, U.C., Knie, K., Rugel, G., Wallner, A., Dillmann, I., Dollinger, G., von Gostomski, C.L., Kossert, K., Maiti, M., Poutivtsev, M., Remmert, A., 2010. A new value for the half-life of ^{10}Be by Heavy-Ion Elastic Recoil Detection and liquid scintillation counting. Nucl. Instrum. Methods Phys. Res., Sect. B, Beam Interact. Mater. Atoms 268, 187–191.

Laj, C., Channell, J.E.T., 2007. Geomagnetic excursions. In: Schubert, G., Kono, M. (Eds.), Treatise in Geophysics, vol. 5: Geomagnetism. Elsevier, Amsterdam, pp. 373–416.

Laj, C., Kissel, C., Beer, J., 2004. High resolution global paleointensity stack since 75 kyr (GLOPIS-75) calibrated to absolute values. In: Channell, J.E.T., Kent, D.V., Lowrie, W., Meert, J.G. (Eds.), Timescales of the Paleomagnetic Field. In: Geophys. Monogr., vol. 145. AGU, Washington D.C., pp. 255–265.

Laj, C., Kissel, C., Mazaud, A., Channell, J.E.T., Beer, J., 2000. North Atlantic paleointensity stack since 75 ka (NAPIS-75) and the duration of the Laschamp event. Philos. Trans. R. Soc. Lond. 358, 1009–1025.

Lal, D., 1988. Theoretically expected variations in the terrestrial cosmic-ray production rates of isotopes. In: Castagnoli, G.C. (Ed.), Proceedings of the International School of Physics "Enrico Fermi," Course XCV. North-Holland, Amsterdam, pp. 216–233.

Langereis, C.G., Dekkers, M.J., DeLange, G.J., Paterne, M., Santvoort, P.J.M., 1997. Magnetostratigraphy and astronomical calibration of the last 1.1 Myr from an eastern Mediterranean piston core and dating of short events in the Brunhes. Geophys. J. Int. 129, 75–94.

Lanphere, M.A., 2000. Comparison of conventional K/Ar and $^{40}Ar/^{39}Ar$ dating of young mafic volcanic rocks. Quat. Res. 53, 294–301.

Legrand, J.-P., 1984. Introduction élémentaire à la physique cosmique et à la physique des relations Soleil-Terre. CNRS-INAG Ed, Paris.

Lisiecki, L.E., Raymo, M.E., 2005. A Pliocene–Pleistocene stack of 57 globally distributed benthic $\delta^{18}O$ record. Paleoceanography 20, 1–17, http://dx.doi.org/10.1029/2004PA001071.

Liu, X.M., Liu, T.S., Liu, C., Chen, M.Y., 1988. The Chinese loess in Xifeng, I. The preliminary study on magnetostratigraphy of a loess profile in Xifeng area, Gansu Province. Geophys. J. Int. 92, 345–348.

Lund, S., Acton, G.D., Clement, B., Okada, M., Williams, T., 2001. Brunhes chron magnetic field excursions recovered from Leg 172 sediments. In: Keigwin, L.D. Rio, D., Acton, G.D., Arnold, E. (Eds.), Proceedings of the ODP Science Research, vol. 172, pp. 1–18 (Online).

Masarik, J., Beer, J., 1999. Simulation of particle fluxes and cosmogenic nuclide production in the Earth's atmosphere. J. Geophys. Res. 104, 12099–12111.

Masarik, J., Beer, J., 2009. An updated simulation of particle fluxes and cosmogenic nuclide production in the Earth's atmosphere. J. Geophys. Res. 114, D1110, http://dx.doi.org/10.1029/2008JD010557.

McFadden, M.A., Peterson, L.C., Bentley, S.J., Dickens, G.R., Droxler, A.W., Opdyke, B., 2006. Role of paleoclimate and paleoceanography in sediment delivery to the Gulf of Papua over the last 300 kyrs based on foraminiferal and organic matter stable isotope records. In: Annual Meeting. Am. Assoc. of Petrol Geol., Houston, TX.

Ménabréaz, L., Bourlès, D.L., Thouveny, N., 2012. Amplitude and timing of the Laschamp geomagnetic dipole low from the global atmospheric ^{10}Be overproduction: Contribution of authigenic ^{10}Be/^{9}Be ratios in west equatorial Pacific sediments. J. Geophys. Res. 117, B11101, http://dx.doi.org/10.1029/2012JB009256.

Ménabréaz, L., Thouveny, N., Bourlès, D.L., Deschamps, P., Hamelin, B., Demory, F., 2011. The Laschamp geomagnetic dipole low expressed as a cosmogenic ^{10}Be atmospheric overproduction at ~ 41 ka. Earth Planet. Sci. Lett. 312, 305–317.

Milliman, J.D., 1995. Sediment discharge to the ocean from small mountainous rivers: The New Guinea example. Geo-Mar. Lett. 15, 127–133.

Muscheler, R., Beer, J., Wagner, G., Laj, C., Kissel, C., Raisbeck, G.M., Yiou, F., Kubik, P.W., 2004. Changes in the carbon cycle during the last deglaciation as indicated by the comparison of ^{10}Be and ^{14}C records. Earth Planet. Sci. Lett. 219, 325–340.

Muscheler, R., Beer, J., Kubik, P.W., Synal, H.A., 2005. Geomagnetic field intensity during the last 60,000 years based on ^{10}Be and ^{36}Cl from the Summit ice cores and ^{14}C. Quat. Sci. Rev. 24, 1849–1860.

Nishiizumi, K., Imamura, M., Caffee, M.W., Southon, J.R., Finkel, R.C., McAninch, J., 2007. Absolute calibration of ^{10}Be AMS standards. Nucl. Instrum. Methods Phys. Res., Sect. B, Beam Interact. Mater. Atoms 258, 403–413.

Quidelleur, X., Gillot, P.Y., Carlut, J., Courtillot, V., 1999. Link between excursions and paleointensity inferred from abnormal field direction recorded at La Palma around 600 ka. Earth Planet. Sci. Lett. 168, 233–242.

Quidelleur, X., Carlut, J., Soler, V., Valet, J.-P., Gillot, P.Y., 2003. The age and duration of the Matuyama-Brunhes transition from new K-Ar data from La Palma (Canary islands) and revisited ^{40}Ar/^{39}Ar ages. Earth Planet. Sci. Lett. 208, 149–163.

Raisbeck, G.M., Yiou, F., Fruneau, M., Loiseaux, J.M., Lieuvin, M., Ravel, J.C., Reyss, J.M., Guichard, F., 1980. ^{10}Be concentration and residence time in the deep ocean. Earth Planet. Sci. Lett. 51 (2), 275–278.

Raisbeck, G.M., Yiou, F., Fruneau, M., Loiseaux, J.M., Lieuvin, M., Ravel, J.C., 1981. Cosmogenic ^{10}Be/^{7}Be as a probe of atmospheric transport processes. Geophys. Res. Lett. 8, 1015–1018.

Raisbeck, G.M., Yiou, F., Bourlès, D., Kent, D.V., 1985. Evidence for an increase in cosmogenic ^{10}Be during a geomagnetic reversal. Nature 315, 315–317.

Raisbeck, G.M., Yiou, F., Jouzel, J., Petit, J.R., Bard, E., Barkov, N.I., 1992. ^{10}Be deposition at Vostok, Antarctica, during the last 50000 years and its relationship to possible cosmogenic production variations during this period. In: Bard, E., Broecker, W.S. (Eds.), The Last Deglaciation: Absolute and Radiocarbon Chronologies, Series I. Glob. Environmental Change 2, pp. 127–139.

Raisbeck, G.M., Yiou, F., Cattani, O., Jouzel, J., 2006. ^{10}Be evidence for the Matuyama–Brunhes geomagnetic reversal in the EPICA Dome C ice core. Nature 444, 82–84.

Roberts, A.P., Winklhofer, M., 2004. Why are geomagnetic excursions not always recorded in sediments? Constraints from post-depositional remanent magnetization lock-in modelling. Earth Planet. Sci. Lett. 227, 345–359.

Robinson, C., Raisbeck, G.M., Yiou, F., Lehman, B., Laj, C., 1995. The relationship between ^{10}Be and geomagnetic field strength records in central North Atlantic sediments during the last 80 ka. Earth Planet. Sci. Lett. 136, 551–557.

Saracco, G., Thouveny, N., Bourlès, D., Carcaillet, J., 2009. Extraction of non-continuous orbital frequencies from noisy insolation data and from palaeoproxy records of geomagnetic intensity using the phase of continuous wavelet transforms. Geophys. J. Int. 176, 767–781.

Schnepp, E., Hradetzky, H., 1994. Combined paleointensity and ^{40}Ar/^{40}Ar age spectrum data from volcanic rocks of the West Eifel field (Germany): Evidence for an early Brunhes geomagnetic excursion. J. Geophys. Res., Solid Earth 99, 9061–9076.

Shackleton, N.J., 1974. Attainment of isotopic equilibrium between ocean water and the benthonic foraminiferal genus Uvigerina: isotopic changes in the ocean during the last glacial. Cent. Natl. Rech. Sci. Colloq. Int. 219, 203–209.

Shackleton, N.J., Berger, A., Peltier, W.R., 1990. An alternative astronomical calibration of the lower Pleistocene timescale based on ODP site 677. Trans. R. Soc. Edinb. Earth Sci. 81, 251–261.

Singer, B.S., Pringle, M.S., 1996. Age and duration of the Matuyama-Brunhes geomagnetic polarity transition from ^{40}Ar/^{39}Ar incremental heating analyses of lavas. Earth Planet. Sci. Lett. 139, 47–61, http://dx.doi.org/10.1016/0012-821X(96)00003-9.

Singer, B.S., Relle, M.K., Hoffman, K.A., Battle, A., Guillou, H., Carracedo, J.C., 2002. Ar/Ar ages from transitionally magnetized lavas on La Palma, Canary Islands and the geomagnetic instability timescale. J. Geophys. Res. 107, 2307, http://dx.doi.org/10.1029/2001JB001613.

Singer, B.S., Hoffman, K.A., Coe, R.S., Brown, L.L., Jicha, B.R., Pringle, M.S., Chauvin, A., 2005. Structural and temporal requirements for geomagnetic field reversal deduced from lava flows. Nature 434, 633–636.

Singer, B.S., Hoffman, K.A., Schnepp, E., Guillou, H., 2008. Multiple Brunhes Chron excursions recorded in the West Eifel (Germany) volcanics: Support for long-held mantle control over the non-axial dipole field. Phys. Earth Planet. Inter. 169, 28–40.

Singer, B.S., Jicha, B.R., Coe, R.S., Mochizuki, N., 2012. An earthtime chronology for the Matuyama-Brunhes geomagnetic field reversal. In: AGU Fall Meeting Abstract V21E-1465274.

Stoner, J.S., Laj, C., Channell, J.E.T., Kissel, C., 2002. South Atlantic and North Atlantic geomagnetic paleointensity stacks (0-80 ka): implications for inter-hemispheric correlation. Quat. Sci. Rev. 21, 1141–1151.

Tauxe, L., 1993. Sedimentary records of relative paleointensity of the geomagnetic field: Theory and practice. Rev. Geophys. 31 (3), http://dx.doi.org/10.1029/93RG01771.

Tauxe, L., Steindorf, J.L., Harris, A.J., 2006. Depositional remanent magnetization: Toward an improved theoretical and experimental foundation. Earth Planet. Sci. Lett. 244, 515–529.

Tauxe, L., Herbert, T., Shackleton, N.J., Kok, Y.S., 1996. Astronomical calibration of the Matuyama Brunhes Boundary: consequences for magnetic remanence acquisition in marine carbonates and the Asian loess sequences. Earth Planet. Sci. Lett. 140, 133–146.

Thouveny, N., Carcaillet, J., Moreno, E., Leduc, G., Nérini, D., 2004. Geomagnetic moment variation and paleomagnetic excursions since 400 kyr BP: a stacked record from sedimentary sequences of the Portuguese margin. Earth Planet. Sci. Lett. 219, 377–396.

Thouveny, N., Bourlès, D.L., Saracco, G., Carcaillet, J.T., Bassinot, F., 2008. Paleoclimatic context of geomagnetic dipole lows and excursions in the Brunhes, clue for an orbital influence on the geodynamo?. Earth Planet. Sci. Lett. 275, 269–284.

Valet, J.-P., 2003. Time variations in geomagnetic intensity. Rev. Geophys. 41 (1), http://dx.doi.org/10.1029/2001RG000104.

Valet, J.-P., Meynadier, L., 1993. Geomagnetic field intensity and reversals during the past four million years. Nature 366, 234–238.

Valet, J.-P., Meynadier, L., Guyodo, Y., 2005. Geomagnetic field strength and reversal rate over the past 2 million years. Nature 435, 802–805.

von Blanckenburg, F., O'Nions, R.K., Belshaw, N.S., Gibb, A., Hein, J.R., 1996. Global distribution of beryllium isotopes in deep ocean water as derived from Fe–Mn crusts. Earth Planet. Sci. Lett. 141 (1–4), 213–226.

Wagner, G., Masarik, J., Beer, J., Baumgartner, S., Imboden, D., Kubik, P.W., Synal, H.A., Suter, M., 2000. Reconstruction of the geomagnetic field between 20 and 60 kyr BP from cosmogenic radionuclides in the GRIP ice core. Nucl. Instrum. Methods Phys. Res., Sect. B, Beam Interact. Mater. Atoms 172, 597–604.

Xuan, C., Channell, J.E.T., 2008. Origin of orbital periods in the sedimentary relative paleointensity records. Phys. Earth Planet. Inter. 169, 140–150.

Yamazaki, T., Oda, H., 2002. Orbital influence on Earth's magnetic field: 100,000-year periodicity in inclination. Science 295, 2435–2438.

Yiou, F., Raisbeck, G.M., Baumgartner, S., Beer, J., Hammer, C., Johnsen, S., Jouzel, J., Kubik, P.W., Lestringuez, J., Stiévenard, M., Sutter, M., Yiou, P., 1997. Beryllium-10 in the Greenland Ice Core Project ice core at Summit, Greenland. J. Geophys. Res. 102, 26783–26794.

Ziegler, L.B., Constable, C.G., Johnson, C.L., Tauxe, L., 2011. PADM2M: a penalized maximum likelihood model of the 0–2 Ma palaeomagnetic axial dipole moment. Geophys. J. Int. 184, 1069–1089, http://dx.doi.org/10.1111/j.1365-246X.2010.04905.x.